Monthly Notices of the ROYAL ASTRONOMICAL SOCIETY

MNRAS **543,** 640–661 (2025) https://doi.org/10.1093/mnras/staf1446
Advance Access publication 2025 August 30

Asteroseismology of HD 23734, HD 68703, and HD 73345 using *K2–TESS* space-based photometry and high-resolution spectroscopy

Santosh Joshi [1]★ Athul Dileep [1,2] Eugene Semenko [3] Mrinmoy Sarkar,[1] Otto Trust [4,5] Peter De Cat [6] Patricia Lampens,[6] Marc-Antoine Dupret,[7] Surath C. Ghosh,[1] David Mkrtichian [3] Mathijs Vanrespaille,[8] Sugyan Parida,[9] Abhay Pratap Yadav [9] Pramod Kumar S.,[10] P. P. Goswami,[11] Muhammed Riyas[12] and Drisya Karinkuzhi[12]

[1]*Aryabhatta Research Institute of Observational Sciences, Manora Peak, Nainital, Uttarakhand-263002, India*
[2]*Department of Applied Physics, M.J.P Rohilkhand University, Bareilly, Uttar Pradesh-243006, India*
[3]*National Astronomical Research Institute of Thailand (NARIT), 260, Moo 4, Don Kaew, Mae Rim 50180, Chiang Mai, Thailand*
[4]*Department of Physics, Mbarara University of Science and Technology, PO Box 1410, Mbarara, Uganda*
[5]*Department of Physics, Faculty of Science, Kyambogo University, PO Box 1, Kyambogo, Uganda*
[6]*Royal Observatory of Belgium, Av. Circulaire 3, B-1180 Uccle, Belgium*
[7]*Space Sciences, Technologies and Astrophysics Research (STAR) Institute, University of Liège, B-4000 Liège, Belgium*
[8]*Institute of Astronomy, KU Leuven, Celestijnenlaan 200D, B-3001 Leuven, Belgium*
[9]*Department of Physics and Astronomy, National Institute of Technology Rourkela, Sector 1, Rourkela-769008, Odisha, India*
[10]*Indian Institute of Astrophysics, Koramangala, Bangalore-560034, India*
[11]*Dakshin Kamrup College, Gauhati University, Assam-781125, India*
[12]*Department of Physics, University of Calicut, Thenhipalam, Malappuram 673635, India*

Accepted 2025 August 27. Received 2025 August 18; in original form 2025 June 4

ABSTRACT

In this paper, we present a comprehensive study of three stars, HD 23734, HD 68703, and HD 73345, which were previously observed as chemically peculiar candidates within the Nainital-Cape survey and reported as null results for the pulsational variability. Frequency analyses of *K2* and *TESS* time-series photometric data reveal the co-existence of rotational modulation and pulsation. We use the spectrum synthesis technique to determine fundamental parameters and chemical composition, which shows that all the three stars are likely to be chemically normal. The evolutionary status of the target stars corresponds to the main-sequence phases and places them within the δ Scuti instability strip of the Hertzsprung–Russell diagram. The line profile variability is observed in all three stars, especially intriguing in HD 68703 and a typical signature of the non-radial pulsation, demands further detailed examination. Using *TESS* photometry, we identified the radial modes of orders $n = 3$ and 4 for HD 23734, $n = 1$, 3, and 4 for HD 68703, and $n = 3$, 4, and 5 for HD 73345. In addition to the presence of pulsation and rotation, HD 73345 exhibits a steady increase in radial velocity that we interpret as the star being likely to be part of a long-period binary system. Finally, we propose an extended campaign aimed for the in-depth spectroscopic and spectropolarimetric study of selected pulsating stars monitored under the Nainital-Cape survey project.

Key words: asteroseismology – stars: chemically peculiar – stars: oscillations.

1 INTRODUCTION

About 10 per cent of upper main-sequence (MS) stars with spectral types ranging from B to F exhibit anomalous intensities of spectral features compared to normal stars of similar spectral types, ages, and populations. Owing to the observed photospheric overabundances of silicon (Si), chromium (Cr), strontium (Sr), europium (Eu), and many other heavy elements, and are classified as chemically peculiar or CP stars (Ghazaryan, Alecian & Hakobyan 2018).

The CP stars are traditionally divided into four subgroups based on their effective temperature, strength of absorption lines, and magnetic field properties: Am/Fm (CP1), Bp/Ap (CP2), HgMn (CP3), and He-weak (CP4) stars (Preston 1974; Paunzen et al. 2021). As our study focuses primarily on Am (metallic-line A-type) and Ap (peculiar A-type) stars, we briefly introduce these two subtypes within the context of this work.

The Am/Fm stars are non-magnetic objects characterized by deficiencies in light elements (e.g. C, N, O, Ca, and Sc) and/or overabundances of Fe-peak elements (e.g. Fe and Cr) and rare-earth elements (Conti 1970; Catanzaro et al. 2019). These A- or early F-type MS stars occupy the same region of the Hertzsprung–Russell (H-R) diagram as chemically normal A-F stars, with effective temperatures in the range of 7000–9000 K. Most of the Am stars are slow rotators with projected rotational velocities ($\upsilon \sin i$) below 150 km s^{-1} and are commonly found in binary

★ E-mail: santosh@aries.res.in

systems with orbital periods ($P_{\rm orb}$) exceeding 1.2 d (Iliev & Budaj 2008).

The Ap stars possess strong magnetic fields and exhibit pronounced overabundances of elements such as Si, Sr, Cr, and Eu. The magnetic fields of Ap stars are generally organized as dipoles and can reach strengths of several tens of kilogauss (Bychkov, Bychkova & Madej 2021), often varying with rotational period (Babcock 1947; Aurière et al. 2007). Although the origin of these fields remains uncertain, they are thought to be fossil in origin, retained from the process of star formation (Braithwaite & Spruit 2004; Aurière et al. 2007).

The axial rotation of CP stars has a powerful impact on various stellar properties. The chemical peculiarities of Am and Ap stars are believed to arise from processes like atomic diffusion, which can work only in a stabilized environment. It is the slow rotation and magnetic field that suppress convective mixing and allow for the selective levitation or gravitational settling of chemical elements in stellar interiors (Michaud 1970; Richer, Michaud & Turcotte 2000). Slow rotation as the main factor of emerging atomic diffusion in Am stars is typically associated with tidal synchronization in binary systems, while in Ap stars, it is attributed to strong magnetic fields (Abt & Snowden 1973; Shore & Adelman 1974; Ghazaryan & Alecian 2016).

None the less, in certain instances, abnormally high rotational velocities have been noted (e.g. Mikulášek et al. 2022). The rotational properties of a few hundred magnetic CP stars have recently been examined in open star clusters by Netopil et al. (2017), and the authors found that the evolution of rotational periods is consistent with the conservation of angular momentum during the MS phase. The coexistence of pulsations, surface chemical inhomogeneities, moderate rotation, and magnetic fields makes Am and Ap stars exceptional laboratories for asteroseismic modelling, offering valuable insights into internal stellar structure and evolutionary processes (Mikulášek et al. 2010; Krtička et al. 2013).

Several ground-based surveys have been conducted in the past to study CP stars, including the Cape and Nainital-Cape Surveys (N-C Survey; Martinez, Kurtz & Kauffmann 1991; Martinez et al. 2001), the SuperWASP[1] Survey (Smalley et al. 2011), ASAS-3[2] (Bernhard et al. 2015), 2MASS[3] (Herdin, Paunzen & Netopil 2016), LAMOST[4] (Hümmerich, Paunzen & Bernhard 2020; Labadie-Bartz et al. 2023), ATLAS Sky Survey (Bernhard et al. 2021), and the ZTF[5] Survey (Hümmerich, Bernhard & Paunzen 2024), to name a few. Thanks to the high-precision, continuous photometric data obtained from space missions such as *BRITE*[6] (Paunzen 2024a), *Kepler* (Hümmerich et al. 2018), *Gaia*[7] (Paunzen 2024c), and *TESS*[8] (Kobzar et al. 2020), where the data acquired by these missions have led to the detection of multiperiodic pulsations in numerous CP stars covered by the δ Scuti (δSct) instability strip in the H-R diagram (Smalley et al. 2017; Holdsworth et al. 2021; Dürfeldt-Pedros et al. 2024), providing valuable data for modelling the pulsation (Joshi & Joshi 2015; Paunzen 2024b). The CP stars have also been searched for and studied in open star clusters by various authors, as they provide strong constraints on their ages and metallicity given that they are assumed to have originated from the same molecular clouds (Faltová et al. 2025). One of the intriguing findings on CP stars in open clusters is that they are of very young ages ($\log t > 6.90$) and located at galactocentric distances up to 11.4 kpc (Paunzen et al. 2005, 2014).

A class of pulsating variables known as δ Sct stars are located near the intersection between the classical instability strip and the MS. They span effective temperatures of $6300 < T_{\rm eff} < 9000$ K, luminosities of $0.6 < \log(L/L_{\odot}) < 2.0$ dex, and masses (M) between 1.5 and 2.5 $M_{\odot}$. These stars can be found in pre-MS stages or just evolving off the MS and exhibit low-order pressure (p) modes with pulsation periods ranging from ∼15 min to ∼8 h (e.g. Rodríguez & Breger 2001; Buzasi et al. 2005; Guzik 2021). The primary excitation mechanisms include the κ-mechanism in the He II ionization zone (Baker & Kippenhahn 1962; Steindl, Zwintz & Müllner 2022) and turbulent pressure in the H ionization layer (Antoci et al. 2014). The δ Sct pulsators represent a particularly intriguing class of variable stars due to their location in the transition region between stars with convective envelopes ($M < 2\,M_{\odot}$) and those with radiative envelopes ($M > 2\,M_{\odot}$). This transitional nature makes them ideal targets for probing the structure of stellar envelopes. However, understanding the mechanisms that drive pulsations and determining mode selection in δ Sct stars remains a significant unresolved challenge in stellar astrophysics, as their masses fall within a regime where convective zones persist in the outer stellar layers. In binary systems, tidal interactions may further influence the pulsation patterns and rotation rates, producing observable effects in light curves and spectra.

The N-C Survey, a collaborative effort between the Aryabhatta Research Institute of Observational Sciences in India and the South African Astronomical Observatory in South Africa, was initiated in the late-1990s to search for short-period pulsations in CP stars belonging to the Northern and Southern hemispheres and led to the discovery and detailed study of the first far-northern roAp star, HD 12098 (Girish et al. 2001; Kurtz et al. 2024). Subsequent time-resolved photometric and spectroscopic observations revealed anomalous pulsations in half a dozen CP stars (Joshi et al. 2003, 2006, 2009, 2010, 2012, 2016, 2017). In the era of space-based photometry, Joshi et al. (2022) discovered HD 73619 as the first CP heartbeat star, lacking tidally induced pulsations. Recently, Sarkar et al. (2024) conducted an asteroseismic analysis of HD 118660 using *TESS* light curves. A series of non-local thermodynamic equilibrium analyses of hot CP stars using data from HESP (Hanle Echelle Spectrograph) and HERMES (High Efficiency and Resolution Mercator Échelle Spectrograph) spectrographs was also carried out by Trust et al. (2020, 2021, 2023). Furthermore, Dileep, Joshi & Kurtz (2024) revisited the variability classification of N-C Survey stars using *TESS* data. To address the spatial resolution limitations of *TESS*, we have also initiated a ground-based search for pulsating CP stars in open clusters (Dileep et al. 2025). These efforts have now expanded into a global collaboration within the field of asteroseismology through various international bilaterals (e.g. *BINA*[9]) and multilaterals research cooperation (e.g. *SAPTARISI*[10]).

In this study, we perform asteroseismic investigation of three multiperiodic δ Sct stars, HD 23734, HD 68703, and HD 73345, using combined space-based photometric observations from the *K2* and *TESS* missions, complemented by multi-epoch spectroscopy from ground-based facilities. The manuscript is organized as

[1]SuperWASP: Super Wide Angle Search for Planets
[2]ASAS: All Sky Automated Survey
[3]2MASS: Two Micron All-Sky Survey
[4]LAMOST: Large Sky Area Multi-Object Fiber Spectroscopic Telescope
[5]ZTF: Zwicky Transient Facility
[6]BRITE: BRIght Target Explorer
[7]GAIA: Global Astrometric Interferometer for Astrophysics
[8]TESS: Transiting Exoplanet Survey Satellite
[9]BINA: Belgo-Indian Network for Astronomy and Astrophysics
[10]SAPTARISI: Search and Follow-up Studies of Time-domain Astronomical Sources using Sky Surveys, BRICS Telescopes and Artificial Intelligence

follows. The criteria for the selection of the sample are given in Section 2. Section 3 describes the photometric observations and frequency analysis, along with an overview of spectroscopic data acquisition and reduction. Section 4 presents a detailed photometric and spectroscopic analysis to derive fundamental parameters and chemical abundances, along with the evolutionary status of the stars. In Section 5, we identify the observed radial pulsation modes, while Section 5.2 provides details on seismic modelling to constrain the basic stellar parameters. Finally, Section 6 summarizes the conclusions drawn from the present study.

2 TARGET SELECTION

The N-C Survey comprises 381 stars, and none of them were observed by the *Kepler* space mission. However, *K2* data are available for eight targets. Of these, five have been classified as rotational variables (Joshi et al. 2022), and three stars – HD 23734, HD 68703, and HD 73345 – have been identified as pulsating stars in the present study.

HD 23734 was listed as a member of the Pleiades cluster based on *Gaia* DR2 and Apache Point Observatory Galactic Evolution Experiment (APOGEE) radial velocity (RV) data (Poovelil et al. 2020). Joshi et al. (2006) considered this star as a CP candidate based on Strömgren photometric indices. The age and metallicity of this cluster are reported as log(Age) = 8.920 and [Fe/H] = −0.12 ± 0.06 (Dias et al. 2021). However, using the *Gaia* DR3 data, Alfonso & García-Varela (2023) excluded HD 23734 from membership of the Pleiades.

HD 68703 is included in the General Catalogue of Ap and Am stars (Renson & Manfroid 2009), where it is listed as an Am star (Mendoza, Gomez & Gonzalez 1978) with the spectral type A8-dD (with 'dD' denoting a δ Delphini-type star; Cowley & Crawford 1971). Its metallicity, derived from LAMOST medium-resolution spectroscopy is [Fe/H] = 0.352 (Zong et al. 2020). Later, HD 68703 has been classified as a non-magnetic star by Kudryavtsev et al. (2006), with a spectral type of F1 IV (Abt & Morrell 1995), and it exhibits ρ Puppis-type peculiarity – characteristic of evolved, pulsating Am stars. Fundamental parameter derived by Dürfeldt-Pedros et al. (2024) are: $T_{\rm eff}$ = 7192 K, log g = 3.8 dex, and log($L/L_{\odot}$) = 1.29. The same authors investigated its *TESS* light curves and detected five radial pulsation modes, although these remain unidentified.

HD 73345, also known as CY Cnc, is a δ Sct star with a reported pulsation period of 0.1 d (Lopez de Coca et al. 1990) while based on the time-series analysis of the *TESS* data, Pamos Ortega et al. (2023) reported 26 frequencies. This is a confirmed member of the Praesepe cluster, which has an estimated age of 759 Myr (Pamos Ortega et al. 2023). HD 73345 was identified as a candidate CP star in the catalogue of Hauck & Mermilliod (1998). Gray & Corbally (2002) reported this star as a mildly peculiar star with slightly strong Ca II K. However, Fossati et al. (2008) listed the fundamental parameters of the star as log($L/L_{\odot}$) = 1.17, $T_{\rm eff}$ = 7993 K, log g= 3.96 dex, and [Fe/H] = 0.26, their abundance analysis concluded that the star is a chemically normal A7V spectral-type star.

3 OBSERVATIONS AND DATA REDUCTION

3.1 *K2* and *TESS* photometry

The *K2* (*Kepler* two wheel; 2014 February 4–2018 September 26) mission surveyed a 105° × 105° region along the ecliptic plane by observing each field for approximately 80 d across 20 different pointings (Howell et al. 2014). The mission provided two data types: short-cadence (1-min) and long-cadence (30-min) photometry, with an angular resolution of 4 arcsec pixel^{-1}, thereby reducing contamination from nearby stars.

Table 1. Summary of the observational details for the target stars observed by the *K2* and *TESS* space missions, including the available campaigns/sectors and the respective cadences for each star.

Star	Mission	Campaigns/ Sectors	Cadence (s)
HD 23734	*K2*	4	1800
	TESS	42, 43, 44	120
	TESS	70, 71	200
HD 68703	*K2*	5, 18	1800
	TESS	44, 45, 46	120
	TESS	71, 72	200
HD 73345	*K2*	5, 18	1800
	TESS	44, 45, 46	120
	TESS	72	200

The *TESS* (Ricker et al. 2015), launched in 2018, is an all-sky photometric survey operating primarily in the Cousins *I* band. It covers 90 per cent of the sky, originally excluding a narrow band along the ecliptic. During its primary mission, *TESS* observed 26 sectors – each spanning 24° × 96° – dividing each hemisphere into 13 sectors and monitoring them sequentially over one year, with each sector observed for approximately 27.4 d. With an angular resolution of 21 arcsec pixel^{-1}, *TESS* data may suffer from spatial blending and contamination from nearby stars. Sector overlaps at high ecliptic latitudes enable the repeated observation of some stars across multiple sectors. The primary data products include short-cadence (2-min) observations for pre-selected targets and full-frame images captured every 30 min for all stars within the field of view. The extended *TESS* mission, initiated on 2020 July 4, introduced higher temporal resolutions, including 20-s, 200-s, and 10-min cadences, allowing for a more detailed re-observation of all sectors.

The details of the data available from different *TESS* sectors and *K2* campaigns are presented in Table 1. The photometric data products were retrieved using the PYTHON package LIGHTKURVE (Lightkurve Collaboration 2018), sourced from the Barbara A. Mikulski Archive for Space Telescopes (MAST).[11] For both the missions, we utilized the Pre-search Data Conditioning Simple Aperture Photometry flux, which has been corrected for instrumental systematics using co-trending basis vectors. Outliers were identified and removed through a combination of visual inspection and sigma clipping. The resulting light curves were then converted to relative millimagnitudes (mmag) and normalized by subtracting the mean magnitude level to centre them around zero.

3.1.1 *Frequency analyses*

The frequency analysis of the light curves was performed using the PERIOD04 programme (Lenz & Breger 2005). Periodograms were computed over a frequency range from zero to the Nyquist frequency, which is considered to be the maximum frequency resolvable in a frequency spectrum and defined as $\nu_{\rm Nq} = \frac{1}{2\Delta t}$, where Δt represents the time sampling interval. For long (Δt = 29.43 min) and short (Δt = 120 s) cadence data, the Nyquist frequencies are approximately 24.27 and 360 d^{-1}, respectively. To minimize aliasing, we combined contiguous sectors while avoiding large gaps in the time-series data.

[11] https://archive.stsci.edu/

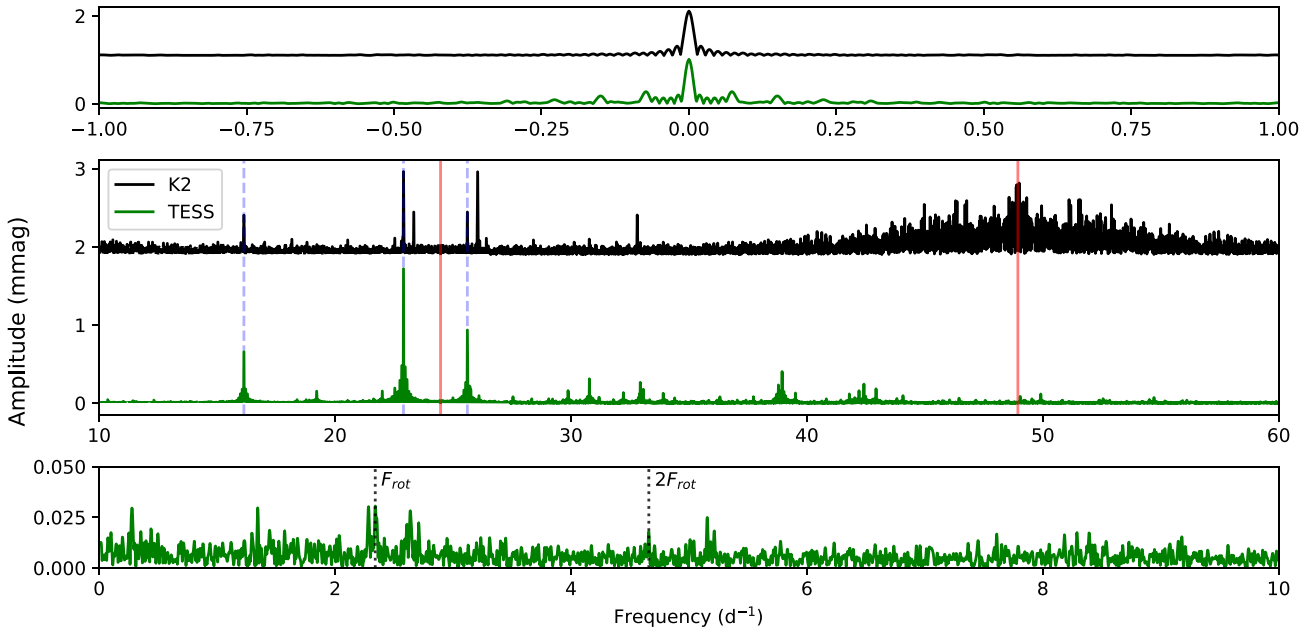

Figure 1. Top panel: the window function for HD 23734 based on photometric data from *K2* (Campaign 4; black) and *TESS* (Sectors 42, 43, and 44; green). Middle panel: comparison of frequency spectra derived from *K2* and *TESS* light curves. For visual clarity, the *K2* spectrum has been vertically shifted by 1.8 mmag. Red vertical solid lines mark the integer multiples of the *K2* Nyquist frequency, while blue dashed lines indicate frequencies common to both missions. Bottom panel: zoomed-in view of the low-frequency range. The black dotted vertical lines denote the rotational frequency and its harmonics.

The resulting frequency spectra were iteratively pre-whitened by fitting the frequency, amplitude, and phase of the highest peak using a sinusoidal model. Each identified frequency was successively subtracted from the light curve, and this process was repeated until the signal-to-noise ratio (SNR) of the residual peaks fell below the significance thresholds, namely SNR < 5.2 for *TESS* data (Baran & Koen 2021), and SNR < 5.7 for *K2* data (Baran, Koen & Pokrzywka 2015). Frequency and amplitude uncertainties were estimated using the formalism described by Montgomery & O'Donoghue (1999). Frequencies separated by less than 2.5 times the Rayleigh resolution ($1/\Delta T$) were considered unresolved (Loumos & Deeming 1978).

Combined frequency spectra of HD 23734, HD 68703, and HD 73345 – based on *K2* campaigns and *TESS* sectors – are presented in Figs 1, 2, and 3, respectively. Individual light curves and periodograms for each *K2* campaign and *TESS* sector are shown in Figs A1–A6 (left and right panels, respectively). A total of 64, 38, and 26 frequencies were recovered in HD 23734, HD 68703, and HD 73345, respectively. It is evident that the short-cadence *TESS* data enabled the detection of more frequencies compared to *K2*. Some of the frequencies were found in one data set (*K2*), but absent in the other (*TESS*) – or vice versa – likely due to the wavelength dependency of pulsation amplitudes. The *K2* band is centred around 6400 Å, while *TESS* operates near 9000 Å. A comparison of the individual amplitude spectra of different *K2* campaigns and *TESS* sectors also revealed amplitude modulations in certain frequencies, potentially caused by beating between close frequencies, non-linear mode coupling, or other non-linear effects (Bowman et al. 2016).

We further searched for possible linear combinations involving radial and rotational frequencies, adopting a relation of the form $aF_n \pm bF_m$, where a and b are integers between -5 and $+5$, and n and m denote the order of the parent radial modes (1, 2, 3, 4, ...) or rotational frequency ('rot'). The identified frequencies, amplitudes, SNR, and their combinations for each target are summarized in Tables B1–B3.

3.2 Spectroscopy

For this study, we employed spectroscopic data obtained from the dedicated observing programmes and various archival sources. High-resolution spectra were acquired using the HESP (Chanumolu, Jones & Thirupathi 2015; Sriram et al. 2018) of the 2.01-m Himalayan Chandra Telescope (HCT) at the Indian Astronomical Observatory (Ladakh, India) and with the HERMES (de Cuyper et al. 2007; Raskin et al. 2011) working with the 1.2-m Mercator Telescope (La Palma, Spain). Medium-resolution spectra were collected for all programme stars with the Medium-Resolution Échelle Spectrograph (MRES) fed by fibre from the 2.4-m Thai National Telescope (TNT) at Doi Inthanon (Chiang Mai, Thailand). One of the programme stars, HD 68703, was observed with MRES and HERMES in a time-series regime.

The raw spectra were reduced using dedicated pipelines specific to each instrument. For HESP and HERMES, those were their respective official pipelines. For the MRES data, we used the latest version of the PYTHON-based pipeline PyYAP.[12]

Wavelength calibration for the medium- and high-resolution spectra was performed using Thorium–Argon (Th-Ar) reference sources, followed by correction for barycentric motion. All spectra were normalized to the continuum level using the CONTINUUM task in the Image Reduction and Analysis Facility (IRAF).[13] The SNR was calculated at a reference wavelength of 5500 Å.

The archival data were found in the European Southern Observatory (ESO) Science Portal,[14] a PolarBase archive of high-resolution

[12]PYTHON-based Yet Another Pipeline (PyYAP): https://github.com/ich-heisse-eugene/PyYAP
[13]https://iraf-community.github.io/
[14]https://archive.eso.org/scienceportal/home

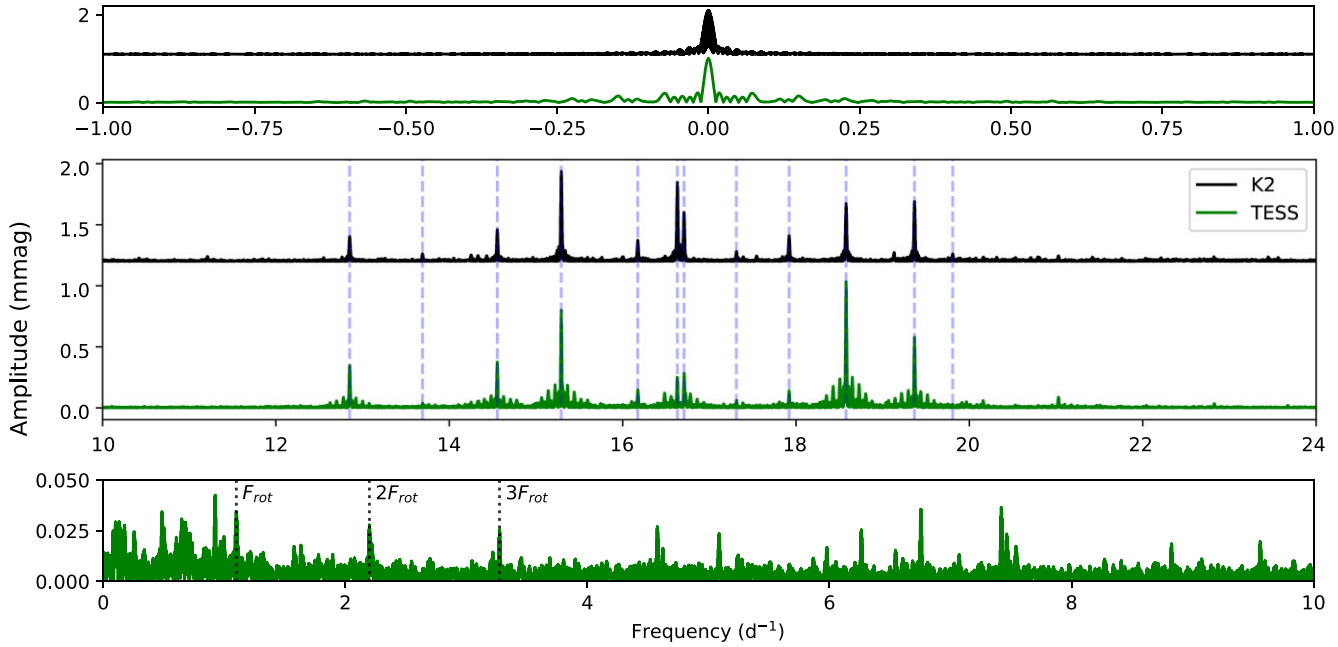

Figure 2. Same as Fig. 1, but for HD 68703 using *TESS* data from Sectors 44, 45, and 46, and *K2* data from Campaigns 5 and 18. All detected frequencies lie within the Nyquist limits of both *K2* and *TESS*.

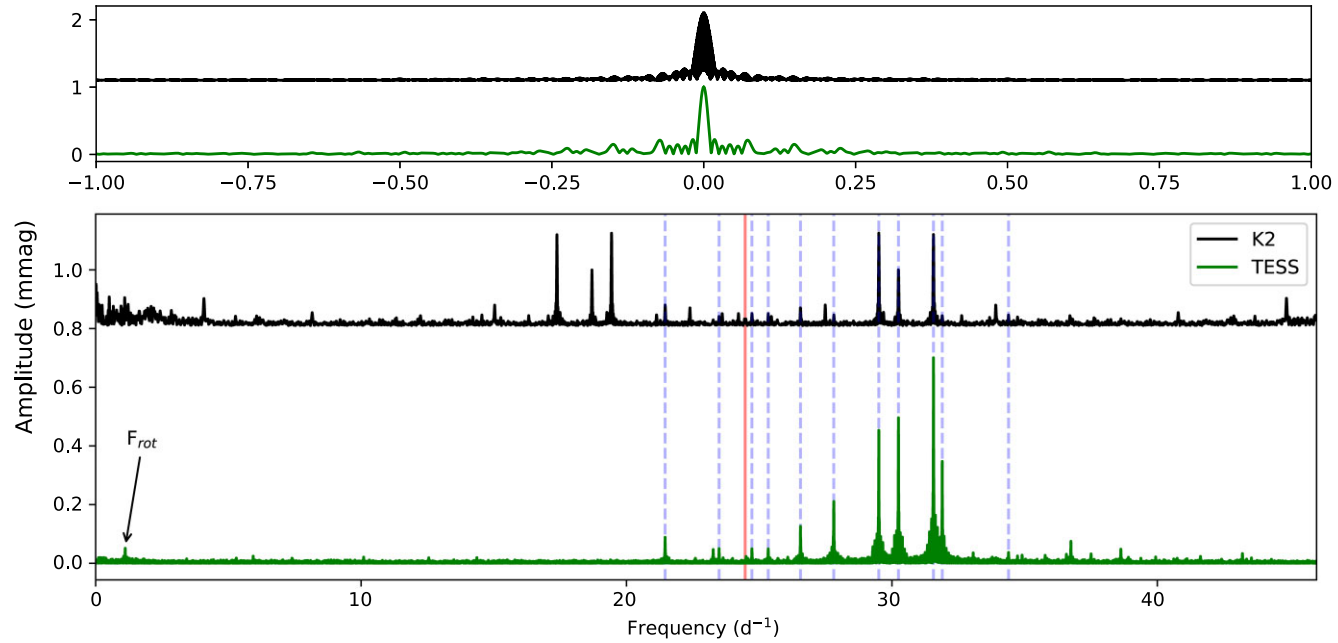

Figure 3. Same as Fig. 1, but for HD 73345 using *TESS* data of Sectors 44, 45, and 46, and *K2* data from Campaigns 5 and 18. The probable rotational frequency is indicated with an arrow.

spectropolarimetric stellar observations[15] (Petit et al. 2014), and in the Data Release 10 (DR10) of the LAMOST archive[16] (Cui et al. 2012; Zhao et al. 2012). Most of these data pertained to HD 68703. This star was observed once with a multiwavelength medium-resolution spectrograph XSHOOTER of the Very Large Telescope (VLT) of ESO under a project ID 110.248M.001. Two observations of HD 68703 resulted in a total of 16 archival spectra from NARVAL, a high-resolution spectropolarimeter of the 2-m Bernard Lyot Telescope (TBL) at the Pic du Midi Observatory, and were acquired from PolarBase. All of our target stars were observed multiple times with the LAMOST, and their spectra were publicly released as part of DR10.

[15] https://www.polarbase.ovgso.fr/
[16] https://www.lamost.org/dr10/v2.0/search

Table 2. Overview of the spectroscopic observations acquired from various ground-based facilities. Asterisks denote the epochs when the time-series spectra were obtained; the listed parameters for those entries represent the values averaged across all individual exposures.

Object	Telescope	Diameter (m)	Spectrograph	Date (UT)	BJD (2400000 +)	Resolution ($\lambda/\Delta\lambda$)	Integration time (s)	SNR (@5500 Å)	RV (km s^{-1})	$\upsilon \sin i$ ($\pm$1 km s^{-1})
HD 23734	LAMOST	4.0	LRS	2018 Jan 16	58135.0181	1800	1800	140	-1.3 ± 3.1	–
				2019 Jan 06	58490.0631	1800	1800	227	-5.8 ± 1.8	–
	HCT	2.01	HESP	2018 Dec 06	58459.3276	30 000	1200	137	-4.8 ± 0.4	133
				2023 Nov 06	60255.1806	30 000	1200	40	-4.6 ± 0.9	134
				2024 Jan 29	60339.2102	30 000	900	75	-4.4 ± 0.7	135
	Mercator	1.20	HERMES	2023 Nov 04	60252.5708	85 000	200	60	-3.4 ± 0.5	132
	TNT	2.4	MRES	2025 Feb 13	60720.0171	18 500	900	170	4.0 ± 1.8	138
HD 68703	VLT UT3	8.2	XSHOOTER	2022 Dec 22	59935.8470	11 333	10	366	0.0 ± 4.5	–
	LAMOST	4.0	MRS	2017 Dec 27	58115.2472	7500	600	164	–	–
				2018 Nov 28	58451.3479	7500	1200	21	–	–
				2018 Dec 19	58472.2812	7500	1200	21	–	–
				2018 Dec 27	58480.3013	7500	1200	41	–	–
				2019 Feb 11	58526.1180	7500	1200	11	–	–
				2021 Jan 04	59219.2638	7500	1200	79	–	–
	HCT	2.01	HESP	2018 Nov 29	58452.4225	30 000	1200	103	-0.3 ± 0.2	69
				2023 Dec 26	60305.2285	30 000	900	222	0.2 ± 0.2	68
				2024 Jan 28	60338.4145	30 000	900	162	0.6 ± 0.2	65
				2025 Mar 07	60742.1224	30 000	900	146	0.8 ± 0.2	68
				2025 Mar 07	60742.3348	30 000	900	168	0.7 ± 0.2	68
	TNT	2.4	MRES	2024 Dec 18*	60663.2273	18 500	410	200	2.3 ± 0.2	69
				2024 Dec 19*	60664.4384	18 500	389	222	1.0 ± 0.2	68
				2025 Feb 13	60720.0672	18 500	420	200	2.6 ± 1.1	67
	TBL	2.0	NARVAL	2007 Jan 12*	54113.6120	65 000	600	266	1.46 ± 0.05	68
				2007 Jan 17*	54118.6024	65 000	600	296	1.45 ± 0.07	68
	Mercator	1.20	HERMES	2025 Mar 15	60750.5739	85 000	300	148	0.9 ± 0.2	68
				2025 Mar 15	60750.5819	85 000	300	173	1.3 ± 0.2	68
				2025 Mar 16	60751.4649	85 000	300	151	1.0 ± 0.2	68
				2025 Mar 16	60751.5914	85 000	300	134	0.9 ± 0.2	67
				2025 Mar 17	60752.4550	85 000	300	183	1.7 ± 0.2	67
				2025 Mar 17	60752.5762	85 000	300	159	1.1 ± 0.1	66
				2025 Mar 18	60753.5355	85 000	300	161	1.2 ± 0.1	65
				2025 Mar 20*	60755.5388	85 000	180	140	1.42 ± 0.02	66
				2025 Mar 23	60758.5722	85 000	360	119	1.5 ± 0.1	66
HD 73345	LAMOST	4.0	LRS	2016 Jan 04	57392.2045	1800	1800	312	24.9 ± 2.1	–
				2016 Jan 27	57415.1631	1800	2100	140	28.4 ± 3.3	–
				2016 Feb 24	57443.1606	1800	1800	255	29.8 ± 2.2	–
	HCT	2.01	HESP	2018 Dec 06	58459.3733	30 000	1200	79	32.5 ± 0.2	90
				2023 Dec 26	60305.2426	30 000	900	55	32.4 ± 0.4	89
				2024 Jan 28	60338.4302	30 000	900	63	33.0 ± 0.3	89
	TNT	2.4	MRES	2025 Feb 13	60720.0945	18 500	900	160	37.1 ± 1.2	90

The details of all spectroscopic observations are summarized in Table 2. Besides the information about the origin and time of the observation, the last three columns of the table list the SNR, RV, and projected rotational velocity ($\upsilon \sin i$) measured from each spectrum.

4 STELLAR FUNDAMENTAL PARAMETERS AND EVOLUTIONARY STATUS

The reliable values of the fundamental stellar parameters, such as effective temperature ($T_{\rm eff}$), surface gravity ($\log g$), metallicity ([M/H]), and rotational characteristics in the form of the projected rotational velocity ($\upsilon \sin i$) or period of axial rotation, are essential for any theoretical modelling. These parameters naturally restrict the range of possible solutions. The following subsections, review the observational approach to the determination of stellar parameters and its outcome for all the target stars.

4.1 Interstellar extinction

The interstellar extinction alters the observed characteristics of the stars. High-resolution spectroscopy of stars in close proximity to the Sun, like objects in our study, is less sensitive to this effect. However, we cannot ignore the reddening when it comes to photometry, which we used for the preliminary evaluation of stellar parameters.

To account for the potential effect of reddening, we first examined the 3D Bayestar dust maps (Green 2018; Green et al. 2019). Using *Gaia* parallaxes (Gaia Collaboration 2018) and galactic coordinates from the SIMBAD database[17] (Wenger et al. 2000), the Bayestar models yielded zero reddening values for all targets in our sample. However, more recent interstellar extinction maps given by Lallement et al. (2022) and Vergely, Lallement & Cox (2022) indicate non-zero cumulative absorption values (A_{5500}, at $\lambda = 5500$ Å) for

[17] https://simbad.u-strasbg.fr/simbad/

Table 3. Basic physical parameters of the target stars retrieved from the SIMBAD database (columns 2–4). The rest of the columns list parameters estimated from photometric calibrations. The distance d is calculated using the *Gaia* DR3 parallax (Gaia Collaboration 2023). Mean photometric values for each star are indicated with an asterisk.

Star	α_{J2000} ($^h\ ^m\ ^s$)	δ_{J2000} ($^\circ\ '\ ''$)	V (±0.01 mag)	A_V (±0.001 mag)	M_v (±0.01 mag)	d (±1 pc)	$T_{\rm eff}$ (±250 K)	log g (±0.20 dex)	[M/H] (±0.20 dex)
HD 23734	03 48 10.59	+ 21 19 44.66	7.96	0.086	2.56	120	7623[1]	4.09[1]	0.12[1]
							7700[2]	–	–
							7660*	4.09*	0.12*
HD 68703	08 14 11.14	+ 17 40 33.43	6.47	0.025	1.55	96	7340[1]	3.86[1]	0.32[1]
							7180[2]	–	–
							7180[3]	4.02[3]	0.32[3]
							7230*	3.93*	0.32*
HD 73345	08 38 37.86	+ 19 59 23.09	8.14	0.039	1.82	184	7710[1]	3.99[1]	0.26[1]
							7300[2]	–	–
							7980[3]	4.49[3]	0.25[3]
							7660*	4.24*	0.26*

Notes. [1] $uvby\beta$. [2] 2MASS. [3] Geneva.

all three stars. Since A_{5500} closely approximates the commonly used extinction parameter $A_{\rm V}$, we accounted for these values in the analysis. Following them, the highest extinction $A_{5500} = 0.086$ mag is observed for HD 23734, while HD 68703 and HD 73345 exhibit A_{5500} equals to 0.025 and 0.039 mag, respectively. We adopted the values of A_{5500} as the upper limit of interstellar reddening $A_{\rm V}$ and used them in the calculation of stellar luminosities listed in Table 3.

A more direct method of estimating reddening involves measuring the equivalent widths of interstellar Na I D1 and D2 lines in high-resolution spectra. Among the three targets, interstellar features near the Na I D1 and D2 lines were securely detected only in HD 23734. The equivalent widths of these features were measured as W_λ(D1) = 100 mÅ and W_λ(D2) = 85 mÅ. Applying the empirical calibration given by Poznanski, Prochaska & Bloom (2012), we derived the colour excess of E_{B-V}, which corresponds to a total extinction of $A_{\rm V} = 0.06$–0.10 mag (assuming $A_{\rm V} = 3.11 \times E_{B-V}$), in a good agreement with the A_{5500} value for this star. There was no measurable interstellar Na I absorption detected in the spectra of HD 68703 or HD 73345.

4.2 Fundamental parameters and chemical composition

4.2.1 Photometry-based evaluation

Before proceeding with spectroscopic analysis, we used Geneva (Golay 1980; Rufener & Nicolet 1988), $uvby\beta$ (Strömgren 1963, 1966; Crawford & Mander 1966; Hauck & Mermilliod 1998), and 2MASS (Cutri et al. 2003) photometry to derive stellar fundamental parameters. By combining colour indices from multiple photometric systems, we aimed to minimize discrepancies arising from potential binarity, which can significantly affect the total flux of the system. Multiple $T_{\rm eff}$ values derived from different indices were averaged, and the results are presented in Table 3, alongside the parameters derived from the other two photometric systems.

In our sample, Geneva photometric indices are available only for HD 68703 and HD 73345 (Paunzen 2022). Applying the calibrations by Kunzli et al. (1997) to the $B2-V1$, d, and $m2$ indices, we obtained $T_{\rm eff} = 7180$ K and log $g = 4.02$ dex for HD 68703, and $T_{\rm eff} = 7980$ K and log $g = 4.50$ dex for HD 73345. For the metallicity [M/H], this calibration yields values in the range of +0.20 to +0.35 dex for both stars. Notably, HD 73345 exhibits an unusually high surface gravity.

Photometric indices of the $uvby\beta$ system are available for all three stars, as compiled by Paunzen (2015). To analyse these, we employed the calibrations developed by Moon & Dworetsky (1985) and refined by Napiwotzki, Schoenberner & Wenske (1993), providing estimates of $T_{\rm eff}$, log g, and [M/H] for the stars under study.

From the 2MASS photometric system, we estimated stellar effective temperatures using the relations given by Casagrande et al. (2021). The photometrically derived parameters were subsequently refined using the spectra.

4.2.2 Spectroscopic approach

In contrast to photometry, spectroscopic analysis offers a more reliable way to determine multiple stellar parameters from just one observation. To evaluate the fundamental parameters and chemical composition of the programme stars, we employed a spectrum-fitting technique.

Our analysis utilized an IDL-based implementation of the SPECTROSCOPY MADE EASY package (SME; Valenti & Piskunov 1996; Piskunov & Valenti 2017) with a grid of built-in ATLAS9 models to fit synthetic spectra to medium- and high-resolution observational data. Line lists were obtained from the Vienna Atomic Line Database (VALD; Piskunov et al. 1995; Kupka et al. 2000; Ryabchikova et al. 2015) based on $T_{\rm eff}$ and log g values estimated from photometry.

Taking the photometric $T_{\rm eff}$, log g, and [M/H] as starting parameters, we refined $T_{\rm eff}$ and [M/H] by fitting the LAMOST (HD 23734 and HD 73345) and XSHOOTER (HD 68703) spectra. We preferred this approach to the direct handling of high-resolution data because the Balmer lines in Échelle spectra of early-type stars typically span a significant fraction of a single order, complicating accurate continuum normalization.

In the subsequent step, we analysed the high-resolution spectra to determine the surface gravity (log g), microturbulence ($\xi_{\rm mic}$), and individual elemental abundances. To do so, $T_{\rm eff}$ was fixed, [M/H] was set to zero, and hydrogen lines were excluded from the fit. All steps of analysis were performed in the local thermodynamic equilibrium (LTE) approach. The final best-fitting spectroscopically derived parameters are presented in Table 4. To demonstrate the goodness of fit, for all the target stars, by the black solid lines in Fig. 4, we plot the regions of spectra obtained with HERMES (HD 23734 and HD 68703), and MRES (HD 73345) and centred at the Balmer lines H_α and H_β. Spectra synthesized with the spectroscopically derived parameters are shown there as red lines. Within the error

Table 4. Summary of stellar parameters derived from spectroscopy.

Star	$T_{\rm eff}$ (K)	$\log g$ [cm s^{-2}]	$\xi_{\rm mic}$ (km s^{-1})	[M/H] (dex)
HD 23734	7670 ± 160	3.98 ± 0.15	2.7 ± 0.5	-0.31 ± 0.10
HD 68703	7160 ± 250	3.40 ± 0.15	2.7 ± 0.3	$+0.12 \pm 0.10$
HD 73345	7670 ± 220	4.08 ± 0.15	3.0 ± 0.3	-0.14 ± 0.12

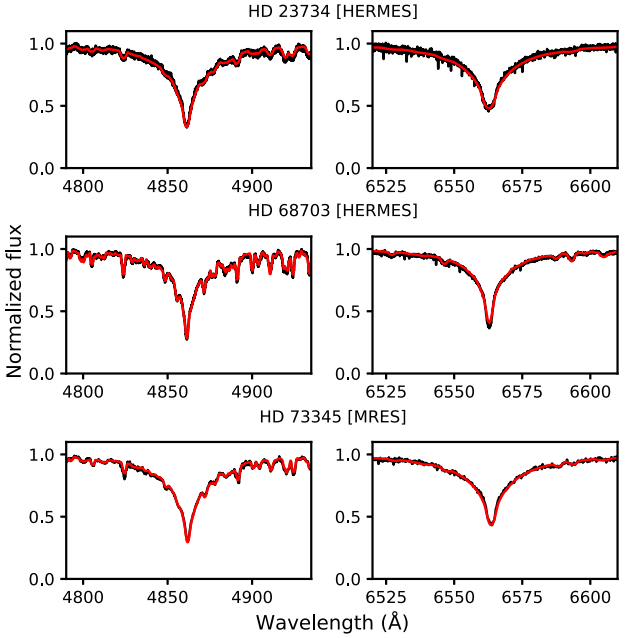

Figure 4. The H_β (left panel) and H_α (right panel) line regions for the target stars. The spectrographs used to obtained these profiles are listed in the top of each panel. The observed and synthetic profiles are shown with black and red colours, respectively.

limits, the spectroscopic parameters agree with the photometric values listed in Table 3.

4.2.3 *Stellar rotation*

The rotational broadening of spectra was estimated using the least-squares deconvolution (LSD) method (Donati & Brown 1997). The line mask required for deconvolution was constructed from VALD line lists, tailored to the derived fundamental parameters of each star. LSD profiles were fitted with a function describing rotational broadening (Gray 2005), with some of the best-fitting profiles shown in Fig. C1. Two parameters, $\upsilon \sin i$ and RV, found in this way are listed in columns 10 and 11 of Table 2. From SME spectrum fitting, the averaged $\upsilon \sin i$ values for HD 23734, HD 68703, and HD 73345 are 134 ± 5, 69 ± 2, and 88 ± 3 km s^{-1}, respectively.

The LSD profiles of HD 23734 and HD 73345 exhibit minimal line profile variability (LPV), likely due to high-order pulsation combined with significant rotational broadening. In contrast, HD 68703 shows substantial LPV which is confidently attributable to pulsational activity, making this star an excellent candidate for detailed follow-up studies.

In photometric time-series, we searched for the rotational frequencies in the range 0.1 to 5 d^{-1} (Balona 2011) as shown in Fig. D1. In this diagram, viable rotational frequencies correspond to positions below the diagonal line representing 90° inclination, as

Table 5. Individual chemical abundances determined for the target stars using HERMES (HD 23734 and HD 68703), and MRES (HD 73345) spectra. The last column lists the solar abundances (Asplund, Amarsi & Grevesse 2021; Magg et al. 2022). The abundances are expressed as $\log(N_{\rm el}/N_{\rm tot})$ with typical uncertainties ($\sigma(\log N/N_{\rm tot})$) between 0.10 and 0.35 dex, except for least accurate values marked with a colon (:).

	HD 23734	HD 68703	HD 73345	Sun
C	−4.23 (:)	−3.65	−3.45	−3.47
O	−2.97 (:)	−2.96 (:)	−2.91 (:)	−3.26
Na	−5.25	−5.44	−5.47	−5.81
Mg	−4.63	−4.22	−4.39	−4.48
Al	−6.09 (:)	−5.37	−5.61 (:)	−5.60
Si	−4.41	−4.40	−4.42	−4.44
S	–	−4.74	–	−4.91
Ca	−5.64	−5.22	−5.60	−5.66
Sc	−9.29	−8.30	−8.75	−8.89
Ti	−7.19	−6.81	−7.12	−7.06
V	−8.02 (:)	–	−7.63	−8.13
Cr	−6.42	−6.21	−6.39	−6.41
Mn	−6.74	−6.74	−6.79	−6.61
Fe	−4.71	−4.45	−4.61	−4.52
Co	–	-	−6.76 (:)	−7.09
Ni	−6.13 (:)	−5.67	−5.82	−5.79
Cu	–	−8.15	–	−7.85
Zn	−7.77 (:)	−7.67	−7.61	−7.47
Sr	−11.05 (:)	−8.48 (:)	–	−9.20
Y	−9.92	−9.26	−9.48	−9.82
Zr	–	-	−9.44 (:)	−9.44
Ba	−9.24	−8.75	−9.67	−9.76
La	–	−10.30	−10.59 (:)	−10.92

$\upsilon \sin i$ must always be less than or equal to the equatorial velocity. For HD 23734, we identified a frequency of 2.3406 d^{-1}, which exhibits one harmonic. Although its S/N ratio falls below the detection threshold of Signal-to-Noise Ratio (SNR) = 5.2, we classify this as a probable rotational frequency. In the case of HD 68703, a frequency of 1.0995 d^{-1} was detected with two harmonics. For HD 73345, we observed a frequency of 1.1119 d^{-1}, although no harmonics were identified. To evaluate the feasibility of the identified rotational frequencies, we estimated equatorial rotational velocities from the computed stellar radii and compared them to the spectroscopic $\upsilon \sin i$ values, indicating that these rotational frequencies are physically plausible. The inferred inclinations are approximately 45° for HD 23734 and HD 73345, while HD 68703 likely has a lower inclination of $\sim 25°$, which requires additional verification.

4.2.4 *Atmospheric abundances*

The photospheric abundances of all dominant elements were evaluated from fitting multiple segments of spectra taken with HERMES (HD 23734 and HD 68703) and MRES (HD 73345) and summarized in Table 5. In Fig. 5, we plotted the chemical composition of stars relative to the Sun with the reference values adopted from Asplund et al. (2021) and Magg et al. (2022). We characterize the overall composition of HD 23734 and HD 73345 as being mildly metal-deficient, unlike the third star, HD 68703, which shows a slight excess of many elements. The revealed difference in metallicity may reflect the individual specific properties of each star.

In the present study, we ignored the effect of departures from the LTE. This fact might stand behind the abnormal excess of oxygen, which was measured from the O I 7771–7775 Å triplet (e.g. Sitnova, Mashonkina & Ryabchikova 2013). Even though the goodness of

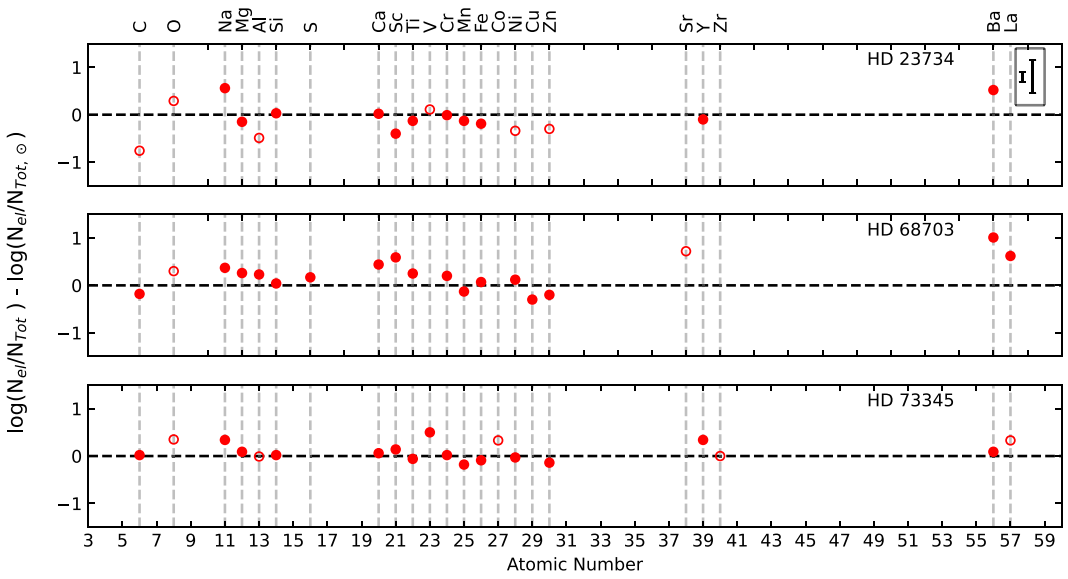

Figure 5. Relative abundances of elements derived from spectroscopic analysis. The horizontal black dashed line indicates solar abundances, while the vertical grey dashed lines mark the one-to-one correspondence between names of the element and respective atomic numbers. The uncertain abundances are designated by the open circles. The box in the upper right corner shows the range (min–max) of the typical error bars (∼ 0.10 to 0.35 dex).

fit is high for the oxygen lines, we marked the derived abundance of this element as uncertain. The low accuracy of the rest of the values marked with a colon in Table 5 mostly resulted from the weakness of measured lines, their limited number, or blending with more abundant species in rotationally broadened profiles.

Our analysis indicates that neither of the programme stars shows strong anomalies typical for CP stars. This conclusion complements the negative test for the presence of a flux depression around 5200 Å (Kupka et al. 2004) in spectra taken with low resolution. We checked for such features in the flux-calibrated low-resolution spectra obtained with LAMOST for HD 23734 and HD 73345, and a medium-resolution spectrum of HD 68703 taken with XSHOOTER. Unfortunately, a flux-calibrated LAMOST spectrum of HD 68703 is unavailable in the LAMOST archive. For comparison, we used *bona fide* CP1 and CP2 stars with a spectral type comparable to that of the target stars. On inspecting the spectra shown in Fig. E1, one can notice that HD 23734 and HD 73345 do not possess any anomalies near 5200 Å. Furthermore, CP1 stars usually exhibit a distinctly weak Ca II K line in their spectra. This line in the spectra of our targets appears normal (Fig. E2), thereby confirming that neither of the studied stars belongs to the Am (CP1) class. In summary, our study portrays HD 23734, HD 68703, and HD 73345 as chemically normal stars.

4.2.5 Stellar multiplicity

We measured the RVs from the available spectra as listed in Table 2. Among the three stars, notably, only HD 73345 showed significant variation of RV over time, suggesting it may be part of a long-period binary system. However, due to the limited temporal sampling of the available data, we were unable to determine the orbital period with confidence, and additional spectroscopic follow-up observations might therefore be essential to confirm the binary status of HD 73345.

In contrast, HD 68703 displays RV variations with a standard deviation of approximately 0.7 km s^{-1}, consistently with rather pulsational variability than binarity. We therefore classify this object as a single star.

4.3 Evolutionary status

To know the evolutionary status of the sample stars, we placed them in the H-R diagram. For this, we used luminosities derived from *Gaia* parallaxes and effective temperatures ($T_{\rm eff}$) obtained from high-resolution spectroscopy. The absolute magnitudes ($M_{\rm V}$) were calculated from the *Gaia* parallaxes (Gaia Collaboration 2016) using the standard relation (Cox 2000). To compute the stellar luminosity ($\log(L/{\rm L}_\odot)$), we adopted a solar bolometric magnitude of $M_{\rm bol,\odot} = 4.73$ mag (Torres 2010). The bolometric correction (BC) was determined using an empirical relation taken from Torres (2010). The resulting values of $M_{\rm V}$ and $\log(L/{\rm L}_\odot)$, along with their associated uncertainties, are listed in Tables 3 and 6, respectively.

The locations of HD 23734, HD 68703, and HD 73345 in the H–R diagram are shown in Fig. 6. It is found that position of HD 23734 is near to the zero-age main sequence (ZAMS) indicates it has recently begun core hydrogen burning. HD 68703 lies near the terminal-age main sequence (TAMS), suggesting that hydrogen in the core is nearly exhausted. HD 73345 is positioned between the ZAMS and TAMS and is likely still undergoing core hydrogen burning.

We have overplotted the stellar evolutionary tracks for masses ranging between 1.6 and 2.0 M$_\odot$, and ages ranging from 0.1 to 1.4 Gyr, computed using the stellar evolution code CLÉS (Code Liégeois d'Evolution Stellaire; Scuflaire et al. 2008a). Theoretical γ Dor (Dupret et al. 2004) and empirical δ Sct (Murphy et al. 2019) instability strips are overlaid for reference. An inspection of the stars' locations within the instability strips, in combination with their frequency spectra, confirms that HD 23734, HD 68703, and HD 73345 are δ Sct-type pulsating variables. It is important to note that the observed values of the luminosity of HD 73345 can be slightly higher than the actual luminosity of the star due to its possible membership to a binary system. If the star has a companion, the

Table 6. Estimated and calculated fundamental parameters derived from the evolutionary status, inferred from the ÉD and best-fitting asteroseismic models for HD 23734, HD 68703, and HD 73345. The parameters reported in the literature are also provided for comparison to the parameters inferred from the present study. The identified frequencies Fn corresponds to the radial fundamental ($n = 1$) and higher overtones ($n > 1$) modes.

	HD 23734			HD 68703			HD 73345		
	Present study			Present study			Present study		
Parameters	Calculated/ H-R diagram	Seismology	Literature	Calculated/ H-R diagram	Seismology	Literature	Calculated/ H-R diagram	Seismology	Literature
$\Delta\nu$ (d^{-1})	6.17 ±0.47	6.96		3.00 ± 0.33	3.25		4.14 ± 0.41	5.20	5.01[b]
$\bar{\rho}/\bar{\rho}_\odot$	0.43±0.07	0.57		0.09 ± 0.02	0.11		0.18 ± 0.04	0.30	
$R_L/R_\odot$	1.57±0.08	–	–	2.79 ± 0.22	–	–	2.17 ± 0.15	–	–
$M/M_\odot$	1.67 ±0.10	–	–	1.96 ± 0.10	–	–	1.85 ± 0.10	–	–
$\log(L/L_\odot)$	0.89 ± 0.01	0.841 ±0.050	–	1.27 ± 0.01	1.175 ± 0.100	1.29[d]	1.17 ± 0.01	1.120 ± 0.050	1.17[g]
$\log(T_{\rm eff})$	3.88±0.01	3.881±0.010	–	3.85 ± 0.02	3.854 ± 0.020	3.86[d]	3.88 ± 0.01	3.899 ± 0.010	3.90[g]
Age (Gyr)	0.5 ± 0.3	0.327±0.010	0.832[c]	1.17 ± 0.10	1.290 ± 0.200	–	1.05 ± 0.10	0.863 ± 0.100	0.759[a]
[Fe/H]	−0.19	–	−0.12[c]	0.07	–	0.352[f]	−0.09	–	0.26[g]
$F1$ (d^{-1})	–	–		9.5603 ± 0.0007	9.56 ± 0.10	–	–	–	
$F2$ (d^{-1})	–	–	–	–	–	–	–	–	–
$F3$ (d^{-1})	32.93878 ± 0.00009	33.01 ± 0.50	–	15.29221 ± 0.00002	15.38 ± 0.20	–	24.7246 ± 0.0005	24.83 ± 0.02	–
$F4$ (d^{-1})	38.94782 ± 0.00006	39.01 ± 0.40	–	18.57798 ± 0.00001	18.46 ± 0.20	–	29.50692 ± 0.00005	29.49 ± 0.01	–
$F5$ (d^{-1})	–	–	–	–	–		34.3951 ± 0.0007	34.25 ± 0.80	–

Note. [a] Alfonso & García-Varela (2023), [b] Pamos Ortega et al. (2023), [c] Dias et al. (2021), [d] Dürfeldt-Pedros et al. (2024), [f] Zong et al. (2020), and [g] Fossati et al. (2008)

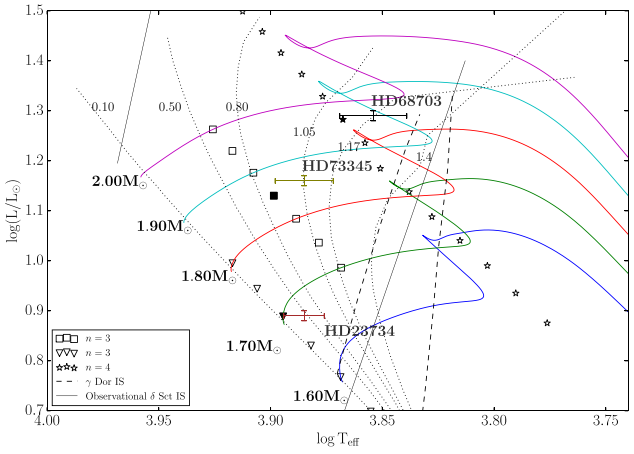

Figure 6. Evolutionary tracks for stellar masses ranging from 1.60 to 2.00 $M_\odot$, computed for solar metallicity ($Z = 0.014$) and overshooting parameter $\alpha_{\rm ov} = 0.1$. Dotted lines denote isochrones corresponding to ages of 0.1, 0.5, 0.8, 1.05, 1.17, and 1.4 Gyr. The open symbols represents seismic models minimizing χ^2 for radial overtone modes: $n = 3$, $f_{T7} = 32.94\,d^{-1}$ for HD 23734 (triangle); $n = 4$, $f_{T1} = 18.58\,d^{-1}$ for HD 68703 (star); and $n = 3$, $f_{T12} = 24.72\,d^{-1}$ for HD 73345 (square) where each model is computed for different stellar masses. The models are consistent with the observations within the 1σ uncertainty box, except for HD 73345 which is likely to be part of a binary system. The solid black lines represent the observational δ Sct instability strip, while the dashed black lines denote the theoretical instability strip of the γ Doradus stars.

combined flux could cause an observed vertical displacement in the H-R diagram, placing HD 73345 above its true evolutionary position.

5 MODE IDENTIFICATION

Asteroseismology leverages stellar pulsation frequencies and their corresponding amplitudes to infer fundamental stellar properties, thereby contributing significantly to our understanding of stellar structure and evolution. A crucial prerequisite for applying asteroseismic techniques is the accurate identification of pulsation modes, which remains a challenging task even when high-precision space-based data are available (Aerts, Christensen-Dalsgaard & Kurtz 2010). In the following subsections, we outline several approaches employed for mode identification in our target stars.

5.1 Échelle diagram

One of the robust techniques for identifying pulsation modes in asteroseismology is the Échelle diagram (ED). In an ED, for a given large frequency separation ($\Delta\nu$), the observed frequencies corresponding to the same angular degree (ℓ) are folded into segments. Frequencies associated with low angular degrees ($\ell < 2$) and high radial orders ($n \gg \ell$) of pressure modes approximately follow the asymptotic relation (Tassoul 1980):

$$\nu_{n,\ell} = \Delta\nu(n + \ell/2 + \epsilon), \tag{1}$$

where n is the radial overtone number, ℓ is the angular degree, and ϵ is a constant of order unity. For higher radial orders, modes of the same degree and consecutive overtone numbers are nearly equally spaced in frequency (Bedding et al. 2020), and this regularity manifests as vertical ridges in the ED.

The large frequency separation $\Delta\nu$ is empirically related to the star's mean density ($\bar{\rho}$) via the following relation (Suárez et al. 2014):

$$\frac{\Delta\nu}{\Delta\nu_\odot} = 0.776 \left(\frac{\bar{\rho}}{\bar{\rho}_\odot}\right)^{0.46}, \tag{2}$$

where $\Delta\nu_\odot = 135\,\mu$Hz $\approx 11.67\,d^{-1}$ is the solar large frequency separation (Huber et al. 2011) and $\bar{\rho}_\odot$ is the mean density of the Sun. To obtain an initial estimate of $\Delta\nu$, we computed the mean stellar density using $\bar{\rho} = M/R^3$, where the radius R was derived from the Stefan–Boltzmann law ($L \propto R^2 T_{\rm eff}^4$) and the mass M was estimated from theoretical evolutionary tracks. These values were then used to refine $\Delta\nu$ through the dynamic Échelle interface (Hey & Ball 2022).

Fig. 7 shows the EDs of HD 23734, HD 68703, and HD 73345, with $\Delta\nu = 6.96$, 3.25, and $5.20\,d^{-1}$, respectively. We identified radial ($\ell = 0$) and possibly non-radial ($\ell = 1$) ridges for all three samples and are highlighted in the figure with light red shaded regions.

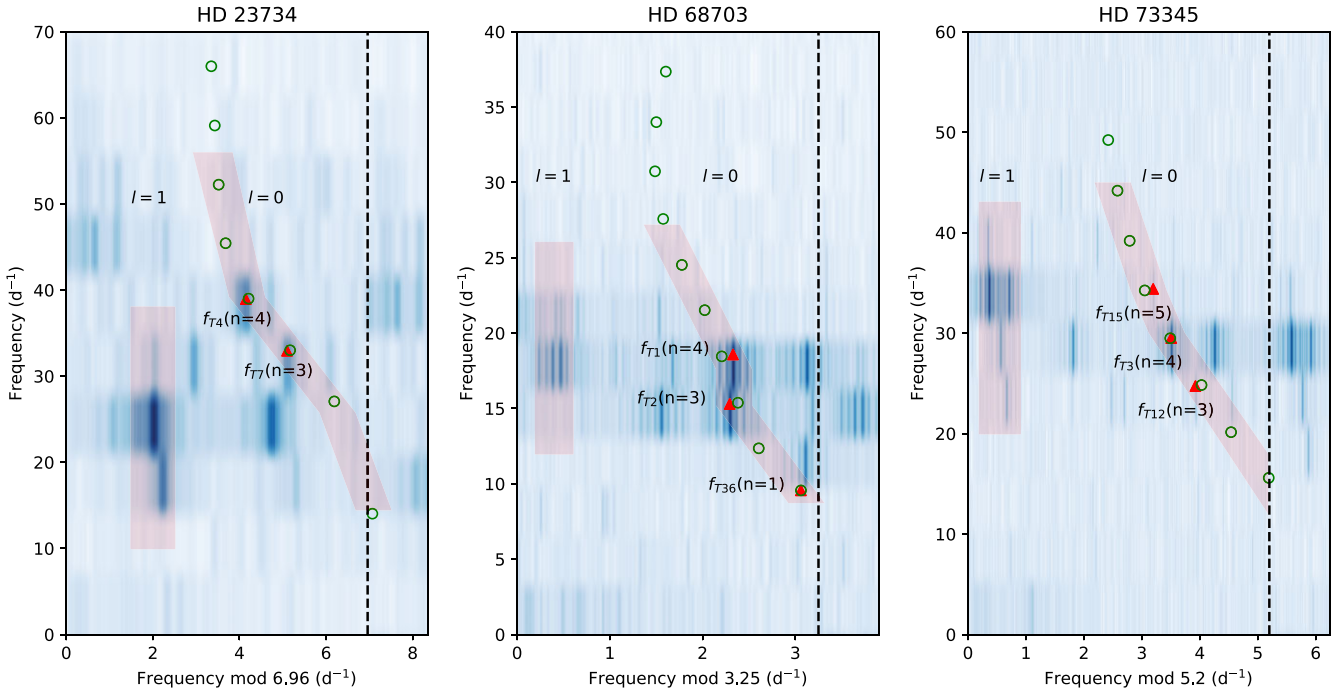

Figure 7. EDs of HD 23734 (left panel), HD 68703 (middle panel), and HD 73345 (right panel), constructed using their respective large frequency separations of $\Delta\nu = 6.96$, 3.25, and 5.20 d^{-1} (indicated by vertical lines). For clarity, the frequency range is extended by 20 per cent beyond the nominal value of $\Delta\nu$. Radial modes predicted by seismic models are shown as open green circles, while observed frequencies are plotted as filled red triangles. The *TESS* frequencies and corresponding radial overtones are denoted by f_T and n, respectively. A notable feature of the Échelle spectra for low- and intermediate-mass pulsators is the appearance of vertical ridges (Bedding et al. 2020), which are visible in all three targets and highlighted by the light red shaded regions.

5.2 Seismic modelling

Seismic modelling is an independent method for accurately measuring the age of stars based on observed frequencies. The conventional approach of employing theoretical isochrones presents considerable uncertainty, particularly near the ZAMS, where the theoretical isochrones are closely spaced.

We adopted an iterative approach to identify the radial pulsation modes using theoretical models. Our working hypothesis assumed that the highest amplitude frequencies ($\nu_{\rm max}^{\rm radial}$) correspond to radial modes of an arbitrary radial order (n) in evolved MS stars, while they correspond to non-radial modes in less evolved stars with a higher surface gravity. To investigate this, we employed the stellar evolution code CLÉS (Scuflaire et al. 2008a) to compute evolutionary models with stellar masses ranging from 1.40 to 2.20 $M_\odot$, assuming solar metallicity ($Z = 0.014$) and a convective core overshooting parameter of $\alpha_{\rm ov} = 0.1$. For each model, we computed the radial mode frequencies ($\ell = 0$) using the adiabatic stellar oscillation code OSC (Scuflaire et al. 2008b), considering various values of the radial overtone number n associated with $\nu_{\rm max}^{\rm radial}$. The most likely n value was determined by minimizing the seismic-χ^2, following the formulation of Murphy et al. (2021):

$$\chi^2 = \left(\frac{f_t - f_o}{\sigma_{f_o}}\right)^2, \tag{3}$$

where f_t and f_o are the theoretical and observed frequencies of the identified radial mode, respectively, and σ_{f_o} is the uncertainty in the observed frequency, taken as 0.1 d^{-1} (Murphy et al. 2021). The best-fitting models for each star were selected based on the minimum χ^2 value, and are overplotted on the H-R diagram and is shown in Fig. 6, alongside evolutionary tracks for various stellar masses. The derived seismic parameters for HD 23734, HD 68703, and HD 73345 are listed in Table 6 and tagged with column seismology.

The identified radial modes that align closely with the models are the second and third overtones for HD 23734; the fundamental, second, and third overtones for HD 68703; and the second, third, and fourth overtones for HD 73345.

5.3 Frequency ratios

When multiple radial modes are present in a pulsating star, the Petersen (1973, 1978) diagram, that depicts the ratio of the higher to lower radial mode frequencies of a star, is generally used to verify the identifications. In this analysis, we compared the theoretical frequency ratios of the higher radial overtones ($n \geq 2$) to the lower radial modes or the fundamental radial mode ($n = 1$) if present. Fig. 8 presents the Petersen diagram for our target stars. These results are in agreement with the mode identifications obtained through the EDs and the seismic models.

5.4 Pulsation constant

To validate the identified radial pulsation modes, we calculated the pulsation constant, Q for each target star, following the formulation provided by Breger (1990). The Q values for HD 23734, HD 68703, and HD 73345 are listed in the fifth columns of Tables B1, B2, and B3, respectively. These values fall within the expected ranges for the fundamental and overtone modes, with fractional uncertainties up to 18 per cent. The adopted Q ranges for radial modes are as follows: fundamental ($Q \geq 0.027$), first overtone ($0.021 \leq Q < 0.027$), second overtone ($0.018 \leq Q < 0.021$), and third overtone ($Q < 0.018$),

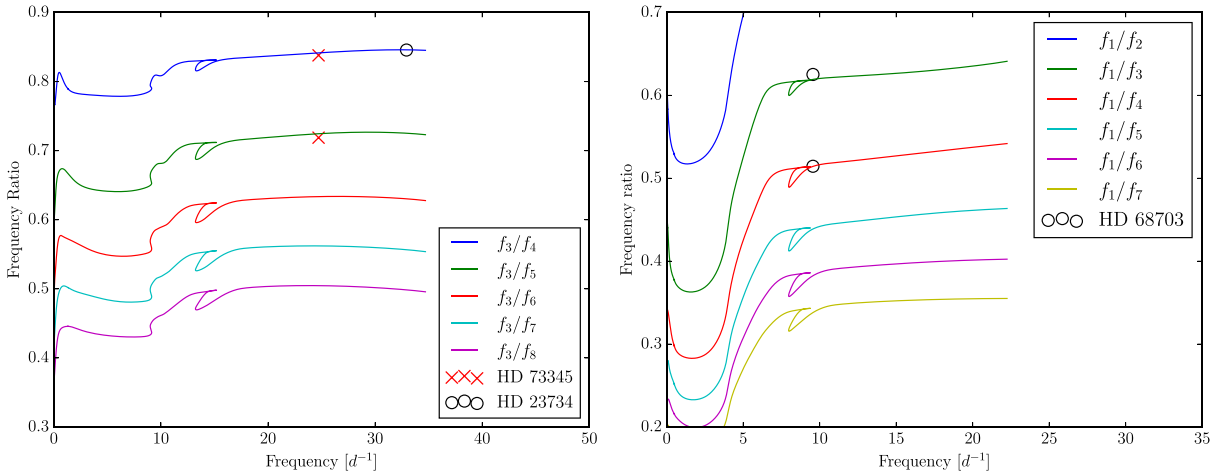

Figure 8. Petersen diagram for HD 23734 and HD 73345 (left panel) and HD 68703 (right panel), computed for $Z = 0.014$ and $\alpha_{ov} = 0.1$. The crosses and circles represent the frequency ratios of the second overtone (f_3) to higher radial overtones for HD 23734 and HD 73345, respectively. For HD 68703, the frequency ratios are calculated for the fundamental (f_1) to higher order modes. The modes identified via frequency ratios show good agreement with those inferred from the EDs.

as given by Poro et al. (2024). The sixth columns of these tables indicate the corresponding identified pulsation modes, labelled as fundamental (F_1) and successive overtones (F_2 to F_5). It is found that HD 23734 pulsates in the second and third overtone, HD 68703 shows pulsations in the fundamental, second, and third overtones and HD 73345 exhibits radial pulsations in the second, third, and fourth overtones. The agreement among the Q values, EDs, seismic models and frequency ratios supports the reliability of the identified radial pulsation modes.

6 CONCLUSIONS AND FUTURE PROSPECTS

The primary goal of the extension of the N-C survey is to gain insights into the interplay between stellar pulsation, chemical inhomogeneities, rotation, and magnetic fields. To achieve the identified goals, we utilized state-of-the-art photometric and spectroscopic data acquired from both ground- and space-based facilities, followed by thorough analyses. Based on our investigation, we draw the following conclusions:

(i) Analysis of *K2* and *TESS* photometry reveals that HD 68703 and HD 73345 are multiperiodic δ Sct pulsators, while HD 23734 is a newly identified δ Sct pulsator. In our studied stars, we have also observed evidence of the coexistence of rotational modulation in the presence of the pulsational variability.

(ii) We have determined the basic astrophysical parameters of HD 23734, HD 68703, and HD 73345 using photometric and spectroscopic data. The lack of anomalies in measured individual abundances, together with the absence of flux depression at 5200 Å in flux-calibrated spectra, confirms that the studied objects are likely to be chemically normal A- and F-type stars.

(iii) The stellar parameters of HD 68703 derived by Dürfeldt-Pedros et al. (2024) are generally consistent with our findings. The LSD profiles of HD 68703 reveal notable line profile variations due to pulsation, making it an ideal candidate for follow-up time-series spectroscopic studies.

(iv) One of the targets, HD 73345, is a member of the Praesepe cluster (Pamos Ortega et al. 2023), which has an estimated age of 759 Myr. This value is relatively close to the 863 Myr derived from our asteroseismic analysis. Pamos Ortega et al. (2023) reported a large frequency separation of $\Delta\nu = 58\mu$Hz (approximately 5.01 d^{-1}) for HD 73345, which is in good agreement with our dynamically derived value of $\Delta\nu = 5.20$ d^{-1}. Further, our RV measurements suggests that HD 73345 is a likely member of a binary system, albeit, the limited phase coverage restricts to make a conclusive results, and demands additional spectroscopic observations to confirm and characterize the system.

(v) Through our comprehensive asteroseismic analysis, we identified the observed radial modes for all three stars. HD 23734 and HD 73345 exhibit predominant non-radial modes, whereas HD 68703 displays prominent radial modes. The observed radial pulsation modes were found to be of radial orders $n = 3$ and 4 for HD 23734; $n = 1$, 3, and 4 for HD 68703; and $n = 3$, 4, and 5 for HD 73345. In addition to the radial modes, we also detected the probable non-radial ridge of $\ell = 1$.

Among the samples observed under the N-C Survey project using ground-based facilities, we have identified several targets that have also been observed by the *TESS* mission (Dileep et al. 2024). These stars were previously classified as non-pulsators based on ground-based observations in the N-C Survey. Therefore, we propose a re-examination of all the objects using high-precision space-based photometry and high-resolution spectroscopy. Thus, the present study is an important step towards finding clues to understand the interactions between pulsation, rotation, binarity, and chemical peculiarities in the intermediate-mass stars.

ACKNOWLEDGEMENTS

The authors acknowledge the anonymous referee for providing the insightful comments. This work is supported by the Belgo-Indian Network for Astronomy and Astrophysics (BINA), approved by the International Division, Department of Science and Technology (DST, Govt. of India; DST/INT/BELG/P-09/2017), and the Belgian Federal Science Policy Office (BELSPO, Govt. of Belgium; BL/33/IN12) (BINA). SJ, SCG, and OT acknowledge the financial support received from the BRICS grant DST/ICD/BRICS/Call-5/SAPTARISI/2023(G). AD acknowledges the financial support received from the DST-INSPIRE Fellowship Programme (DST/INSPIREFellowship/2020/IF200245). OT

acknowledges financial support from the Uppsala University International Science Programme (ISP), the SEISMIC project, and the Max Planck–Humboldt Research Unit, in collaboration with MPA, MPS, and Kyambogo University. SJ, APY, and SP gratefully acknowledge the financial support from the Core Research Grant (CRG/2021/007772) of the Science and Engineering Research Board (SERB), India. This paper includes data collected by the *Kepler* and *TESS* missions, available from the Mikulski Archive for Space Telescopes (MAST), operated by NASA. Based on observations made with the Mercator Telescope, operated on the island of La Palma by the Flemish Community at the Spanish Observatorio del Roque de los Muchachos of the Instituto de Astrofísica de Canarias. Based on observations obtained with the HERMES spectrograph, which is supported by the Research Foundation—Flanders (FWO), Belgium; the Research Council of KU Leuven, Belgium; the Fonds National de la Recherche Scientifique (F.R.S.-FNRS), Belgium; the Royal Observatory of Belgium; the Observatoire de Genève, Switzerland; and the Thüringer Landessternwarte Tautenburg, Germany. Guoshoujing Telescope (the Large Sky Area Multi-Object Fiber Spectroscopic Telescope, LAMOST) is a National Major Scientific Project built by the Chinese Academy of Sciences. Funding for the project has been provided by the National Development and Reform Commission. LAMOST is operated and managed by the National Astronomical Observatories, Chinese Academy of Sciences. The LAMOST spectra are available at https://www.lamost.org/. Part of the research is based on data obtained from the European Southern Observatory (ESO) Science Archive Facility with DOI(s): https://doi.org/10.18727/archive/24, https://doi.org/10.18727/archive/50, and https://doi.org/10.18727/archive/71 under ESO Prog ID 110.248M.001. This research has used data, tools, or materials developed as part of the EXPLORE project, which has received funding from the European Union's Horizon 2020 research and innovation programme under grant agreement no. 101004214.

DATA AVAILABILITY

The high-resolution spectroscopic data used in this article will be shared upon reasonable request to the corresponding author. The *TESS* time-series flux data for the target stars are publicly available from the NASA MAST archive (https://mast.stsci.edu/portal/Mashup/Clients/Mast/Portal.html). This work has made use of data from the European Space Agency (ESA) mission *Gaia* (https://www.cosmos.esa.int/gaia), processed by the Gaia Data Processing and Analysis Consortium (DPAC, https://www.cosmos.esa.int/web/gaia/dpac/consortium). Funding for DPAC has been provided by national institutions, in particular those participating in the *Gaia* Multilateral Agreement. This research has also made use of the SIMBAD database, operated at CDS, Strasbourg, France.

REFERENCES

Abt H. A., Morrell N. I., 1995, ApJS, 99, 135
Abt H. A., Snowden M. S., 1973, ApJS, 25, 137
Aerts C., Christensen-Dalsgaard J., Kurtz D. W., 2010, in Astronomy and Astrophysics Library, Asteroseismology. Springer + Business Media B. V., Germany
Alfonso J., García-Varela A., 2023, A&A, 677, A163
Antoci V. et al., 2014, ApJ, 796, 118
Asplund M., Amarsi A. M., Grevesse N., 2021, A&A, 653, A141
Aurière M. et al., 2007, A&A, 475, 1053
Babcock H. W., 1947, ApJ, 105, 105
Baker N., Kippenhahn R., 1962, Z. Astrophys., 54, 114
Balona L. A., 2011, MNRAS, 415, 1691
Baran A. S., Koen C., 2021, Acta Astron., 71, 113
Baran A. S., Koen C., Pokrzywka B., 2015, MNRAS, 448, L16
Bedding T. R. et al., 2020, Nature, 581, 147
Bernhard K., Hümmerich S., Otero S., Paunzen E., 2015, A&A, 581, A138
Bernhard K., Hümmerich S., Paunzen E., Supíková J., 2021, MNRAS, 506, 4561
Bowman D. M., Kurtz D. W., Breger M., Murphy S. J., Holdsworth D. L., 2016, MNRAS, 460, 1970
Braithwaite J., Spruit H. C., 2004, Nature, 431, 819
Breger M., 1990, Delta Scuti Star Newsl., 2, 13
Buzasi D. L. et al., 2005, ApJ, 619, 1072
Bychkov V. D., Bychkova L. V., Madej J., 2021, Astron. Astrophys. Trans., 32, 137
Casagrande L. et al., 2021, MNRAS, 507, 2684
Catanzaro G., Busà I., Gangi M., Giarrusso M., Leone F., Munari M., 2019, MNRAS, 484, 2530
Chanumolu A., Jones D., Thirupathi S., 2015, Exp. Astron., 39, 423
Conti P. S., 1970, PASP, 82, 781
Cowley A. P., Crawford D. L., 1971, PASP, 83, 296
Cox A. N., 2000, Allen's Astrophysical Quantities. Springer, New York
Crawford D. L., Mander J., 1966, AJ, 71, 114
Cui X.-Q. et al., 2012, Res. Astron. Astrophys., 12, 1197
Cutri R. M. et al., 2003, VizieR Online Data Catalog, University of Massachusetts and Infrared Processing and Analysis Centre (IPAC/Calfornia Institute of Technology), II/246
de Cuyper J. P., Hensberge H., Raskin G., van Winckel H., Lehmann H., Winkler J., Laux U., 2007, in Shaw R. A., Hill F., Bell D. J., eds, ASP Conf. Ser. Vol. 376, Astronomical Data Analysis Software and Systems XVI. Astron. Soc. Pac., San Fransisco, p. 653
Dias W. S., Monteiro H., Moitinho A., Lépine J. R. D., Carraro G., Paunzen E., Alessi B., Villela L., 2021, MNRAS, 504, 356
Dileep A., Joshi S., Kurtz D. W., 2024, Bull. Soc. R. Sci. Liege, 93, 227
Dileep A. et al., 2025, MNRAS, 538, 1747
Donati J.-F., Brown S. F., 1997, A&A, 326, 1135
Dupret M. A., Grigahcène A., Garrido R., Gabriel M., Scuflaire R., 2004, A&A, 414, L17
Dürfeldt-Pedros O., Antoci V., Smalley B., Murphy S., Posilek N., Niemczura E., 2024, A&A, 690, A104
Faltová N. et al., 2025, MNRAS, 536, 72
Fossati L., Bagnulo S., Landstreet J., Wade G., Kochukhov O., Monier R., Weiss W., Gebran M., 2008, A&A, 483, 891
Gaia Collaboration, 2016, A&A, 595, A2
Gaia Collaboration, 2018, A&A, 616, A1
Gaia Collaboration, 2023, A&A, 674, A1
Ghazaryan S., Alecian G., 2016, MNRAS, 460, 1912
Ghazaryan S., Alecian G., Hakobyan A. A., 2018, MNRAS, 480, 2953
Girish V. et al., 2001, A&A, 380, 142
Golay M., 1980, Vistas Astron., 24, 141
Gray D. F., 2005, The Observation and Analysis of Stellar Photospheres, 3rd edn. Cambridge Univ. Press, UK
Gray R. O., Corbally C. J., 2002, AJ, 124, 989
Green G. M., 2018, J. Open Source Softw., 3, 695
Green G. M., Schlafly E. F., Zucker C., Speagle J. S., Finkbeiner D. P., 2019, ApJ, 887, 93
Guzik J. A., 2021, Front. Astron. Space Sci., 8, 55
Hauck B., Mermilliod M., 1998, A&AS, 129, 431
Herdin A., Paunzen E., Netopil M., 2016, A&A, 585, A67
Hey D., Ball W., 2022, Astrophysics Source Code Library, record ascl:2207.005
Holdsworth D. L. et al., 2021, MNRAS, 506, 1073
Howell S. B. et al., 2014, PASP, 126, 398
Huber D. et al., 2011, ApJ, 743, 143
Hümmerich S. et al., 2018, A&A, 619, A98
Hümmerich S., Paunzen E., Bernhard K., 2020, A&A, 640, A40
Hümmerich S., Bernhard K., Paunzen E., 2024, A&A, 692, A231
Iliev I. K., Budaj J., 2008, Contrib. Astron. Obs. Skalnate Pleso, 38, 129
Joshi S., Joshi Y. C., 2015, J. Astrophys. Astron., 36, 33
Joshi S. et al., 2003, MNRAS, 344, 431

Joshi S., Mary D. L., Martinez P., Kurtz D. W., Girish V., Seetha S., Sagar R., Ashoka B. N., 2006, A&A, 455, 303
Joshi S., Mary D. L., Chakradhari N. K., Tiwari S. K., Billaud C., 2009, A&A, 507, 1763
Joshi S., Ryabchikova T., Kochukhov O., Sachkov M., Tiwari S. K., Chakradhari N. K., Piskunov N., 2010, MNRAS, 401, 1299
Joshi S. et al., 2012, MNRAS, 424, 2002
Joshi S. et al., 2016, A&A, 590, A116
Joshi S., Semenko E., Moiseeva A., Sharma K., Joshi Y. C., Sachkov M., Singh H. P., Yerra B. K., 2017, MNRAS, 467, 633
Joshi S. et al., 2022, MNRAS, 510, 5854
Kobzar O. et al., 2020, in Wade G., Alecian E., Bohlender D., Sigut A., eds, Proc. Polish Astronomical Society, Vol. 11, Stellar Magnetism: A Workshop in Honour of the Career and Contributions of John D. Landstreet. Polish Astronomical Society, p. 214
Krtička J., Janík J., Marková H., Mikulášek Z., Zverko J., Prvák M., Skarka M., 2013, A&A, 556, A18
Kudryavtsev D. O., Romanyuk I. I., Elkin V. G., Paunzen E., 2006, MNRAS, 372, 1804
Kunzli M., North P., Kurucz R. L., Nicolet B., 1997, A&AS, 122, 51
Kupka F. G., Ryabchikova T. A., Piskunov N. E., Stempels H. C., Weiss W. W., 2000, Balt. Astron., 9, 590
Kupka F., Paunzen E., Iliev I. K., Maitzen H. M., 2004, MNRAS, 352, 863
Kurtz D. W., Saio H., Holdsworth D. L., Joshi S., Seetha S., 2024, MNRAS, 529, 556
Labadie-Bartz J., Hümmerich S., Bernhard K., Paunzen E., Shultz M. E., 2023, A&A, 676, A55
Lallement R., Vergely J. L., Babusiaux C., Cox N. L. J., 2022, A&A, 661, A147
Lenz P., Breger M., 2005, Commun. Asteroseism., 146, 53
Lightkurve Collaboration, 2018, Astrophysics Source Code Library, record ascl soft:1812.013
Lopez de Coca P., Rolland A., Rodriguez E., Garrido R., 1990, A&AS, 83, 51
Loumos G. L., Deeming T. J., 1978, Ap&SS, 56, 285
Magg E. et al., 2022, A&A, 661, A140
Martinez P., Kurtz D. W., Kauffmann G. M., 1991, MNRAS, 250, 666
Martinez P. et al., 2001, A&A, 371, 1048
Mendoza E. E., Gomez V. T., Gonzalez S., 1978, AJ, 83, 606
Michaud G., 1970, ApJ, 160, 641
Mikulášek Z., Krtička J., Henry G. W., de Villiers S. N., Paunzen E., Zejda M., 2010, A&A, 511, L7
Mikulášek Z., Semenko E., Paunzen E., Hümmerich S., North P. L., Bernhard K., Krtička J., Janík J., 2022, A&A, 668, A159
Montgomery M. H., O'Donoghue D., 1999, Delta Scuti Star Newsl., 13, 28
Moon T. T., Dworetsky M. M., 1985, MNRAS, 217, 305
Murphy S. J., Hey D., Van Reeth T., Bedding T. R., 2019, MNRAS, 485, 2380
Murphy S. J., Joyce M., Bedding T. R., White T. R., Kama M., 2021, MNRAS, 502, 1633
Napiwotzki R., Schoenberner D., Wenske V., 1993, A&A, 268, 653
Netopil M., Paunzen E., Hümmerich S., Bernhard K., 2017, MNRAS, 468, 2745
Pamos Ortega D., Mirouh G. M., García Hernández A., Suárez Yanes J. C., Barceló Forteza S., 2023, A&A, 675, A167
Paunzen E., 2015, A&A, 580, A23
Paunzen E., 2022, A&A, 661, A89
Paunzen E., 2024a, in The BRITE Side of Stars. Celebrating the 10th Anniversary of BRITE Constellation. Zenodo, Vienna, Austria, p. 50
Paunzen E., 2024b, in de Grijs R., Whitelock P. A., Catelan M., eds, Proc. IAU Symp. 376, Pulsation of Chemically Peculiar Stars. Cambridge Univ. Press, p. 91
Paunzen E., 2024c, A&A, 683, L7
Paunzen E., Netopil M., Iliev I. K., Maitzen H. M., Claret A., Pintado O. I., 2005, A&A, 443, 157
Paunzen E., Netopil M., Maitzen H. M., Pavlovski K., Schnell A., Zejda M., 2014, A&A, 564, A42
Paunzen E., Supíková J., Bernhard K., Hümmerich S., Prišegen M., 2021, MNRAS, 504, 3758
Petersen J. O., 1973, A&A, 27, 89
Petersen J. O., 1978, A&A, 62, 205
Petit P., Louge T., Théado S., Paletou F., Manset N., Morin J., Marsden S. C., Jeffers S. V., 2014, PASP, 126, 469
Piskunov N., Valenti J. A., 2017, A&A, 597, A16
Piskunov N. E., Kupka F., Ryabchikova T. A., Weiss W. W., Jeffery C. S., 1995, A&AS, 112, 525
Poovelil V. J. et al., 2020, ApJ, 903, 55
Poro A. et al., 2024, Res. Astron. Astrophys., 24, 025011
Poznanski D., Prochaska J. X., Bloom J. S., 2012, MNRAS, 426, 1465
Preston G. W., 1974, ARA&A, 12, 257
Raskin G. et al., 2011, A&A, 526, A69
Renson P., Manfroid J., 2009, A&A, 498, 961
Richer J., Michaud G., Turcotte S., 2000, ApJ, 529, 338
Ricker G. R. et al., 2015, J. Astron. Telesc. Instrum. Syst., 1, 014003
Rodríguez E., Breger M., 2001, A&A, 366, 178
Rufener F., Nicolet B., 1988, A&A, 206, 357
Ryabchikova T., Piskunov N., Kurucz R. L., Stempels H. C., Heiter U., Pakhomov Y., Barklem P. S., 2015, Phys. Scr, 90, 054005
Sarkar M. et al., 2024, MNRAS, 534, 3211
Scuflaire R., Théado S., Montalbán J., Miglio A., Bourge P. O., Godart M., Thoul A., Noels A., 2008a, Ap&SS, 316, 83
Scuflaire R., Montalbán J., Théado S., Bourge P. O., Miglio A., Godart M., Thoul A., Noels A., 2008b, Ap&SS, 316, 149
Shore S. N., Adelman S. J., 1974, ApJ, 191, 165
Sitnova T. M., Mashonkina L. I., Ryabchikova T. A., 2013, Astron. Lett., 39, 126
Smalley B. et al., 2011, A&A, 535, A3
Smalley B. et al., 2017, MNRAS, 465, 1
Sriram S. et al., 2018, in Evans C. J., Simard L., Takami H., eds, Proc. SPIE Conv. Ser. Vol. 10702, Ground-based and Airborne Instrumentation for Astronomy VII. SPIE, Bellingham, p. 107026K
Steindl T., Zwintz K., Müllner M., 2022, A&A, 664, A32
Strömgren B., 1963, Q. J. R. Astron. Soc., 4, 8
Strömgren B., 1966, ARA&A, 4, 433
Suárez J. C., García Hernández A., Moya A., Rodrigo C., Solano E., Garrido R., Rodón J. R., 2014, A&A, 563, A7
Tassoul M., 1980, ApJS, 43, 469
Torres G., 2010, AJ, 140, 1158
Trust O., Jurua E., De Cat P., Joshi S., 2020, MNRAS, 492, 3143
Trust O., Jurua E., De Cat P., Joshi S., Lampens P., 2021, MNRAS, 504, 5528
Trust O., Mashonkina L., Jurua E., De Cat P., Tsymbal V., Joshi S., 2023, MNRAS, 524, 1044
Valenti J. A., Piskunov N., 1996, A&AS, 118, 595
Vergely J. L., Lallement R., Cox N. L. J., 2022, A&A, 664, A174
Wenger M. et al., 2000, A&AS, 143, 9
Zhao G., Zhao Y.-H., Chu Y.-Q., Jing Y.-P., Deng L.-C., 2012, Res. Astron. Astrophys., 12, 723
Zong W. et al., 2020, ApJS, 251, 15

APPENDIX A: *TESS* AND *K2* LIGHT CURVES AND AMPLITUDE SPECTRA

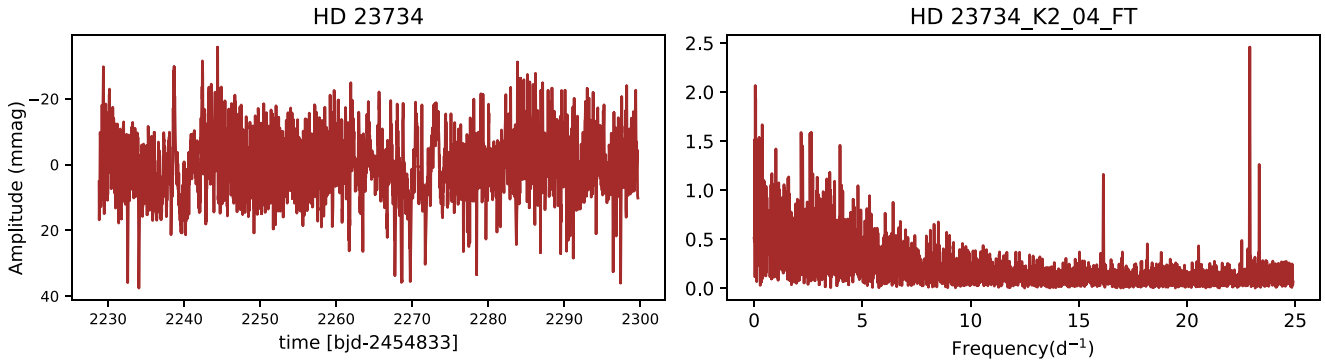

Figure A1. The light curve (left panel) and corresponding frequency spectrum (right panel) for HD 23734 obtained with *K2* during Campaign 4.

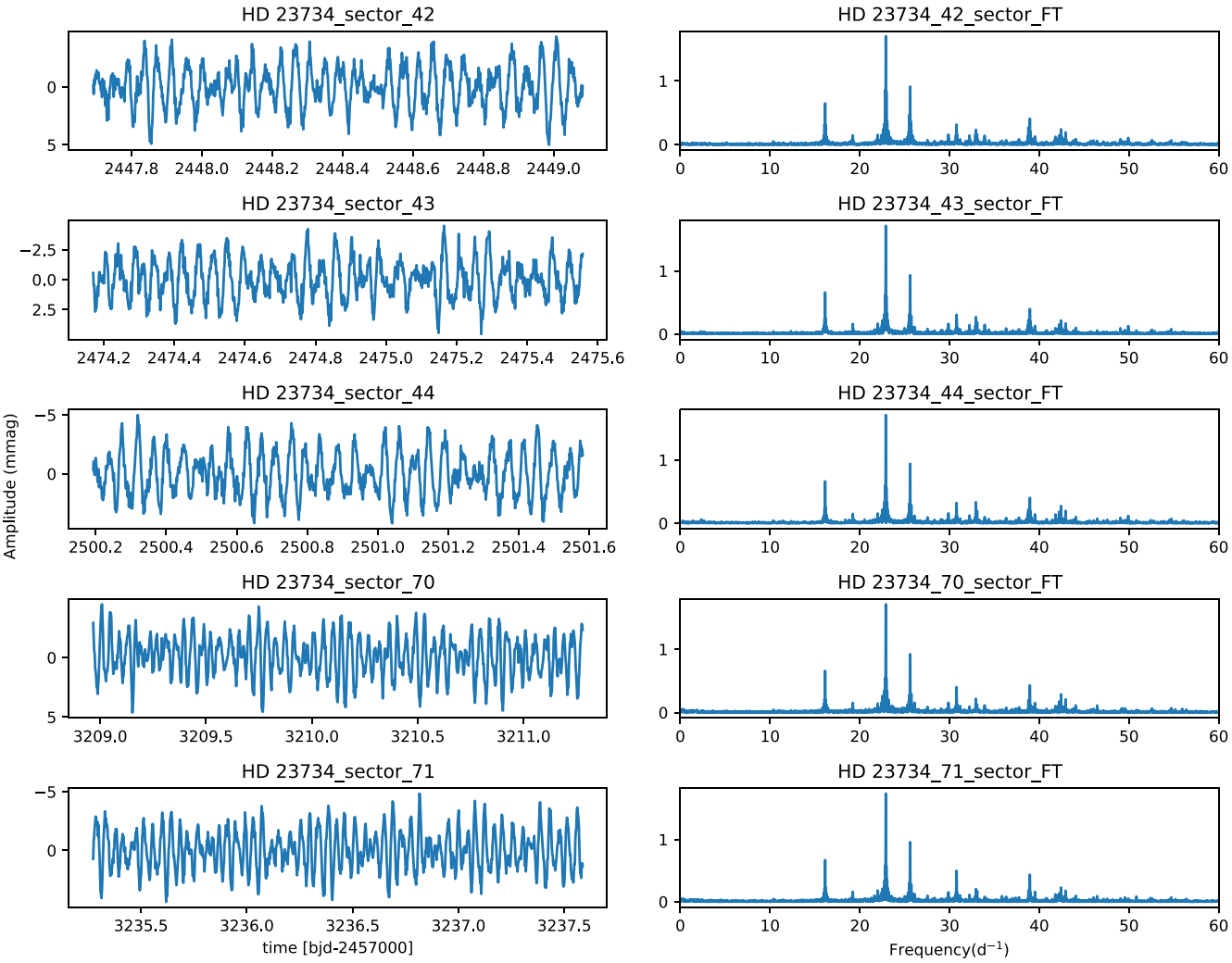

Figure A2. The light curves (left panels) and corresponding frequency spectra (right panels) for HD 23734 obtained with *TESS* in Sectors 42, 43, 70, and 71 (from top to bottom row). The frequency spectra are depicted only up to 60 d^{-1} as no significant frequencies were found beyond this point.

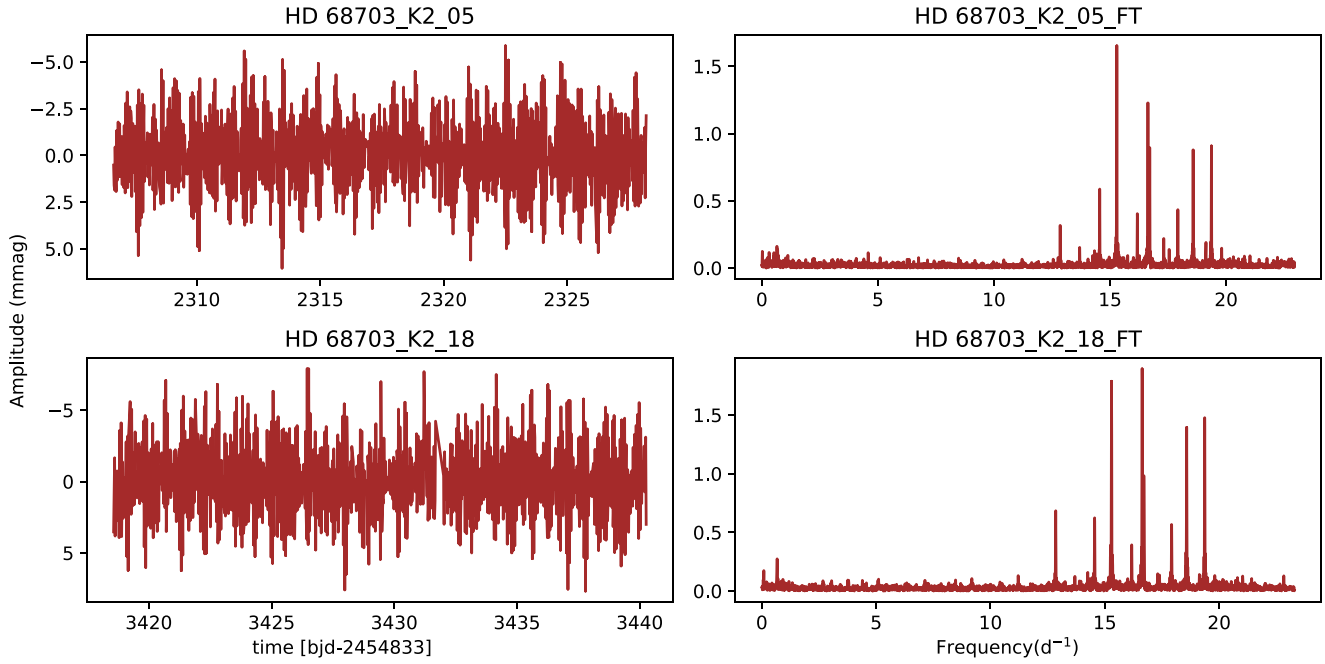

Figure A3. The light curves (left panels) and corresponding frequency spectra (right panels) for HD 68703 obtained with *K2* during Campaign 5 (top row) and Campaign 18 (bottom row).

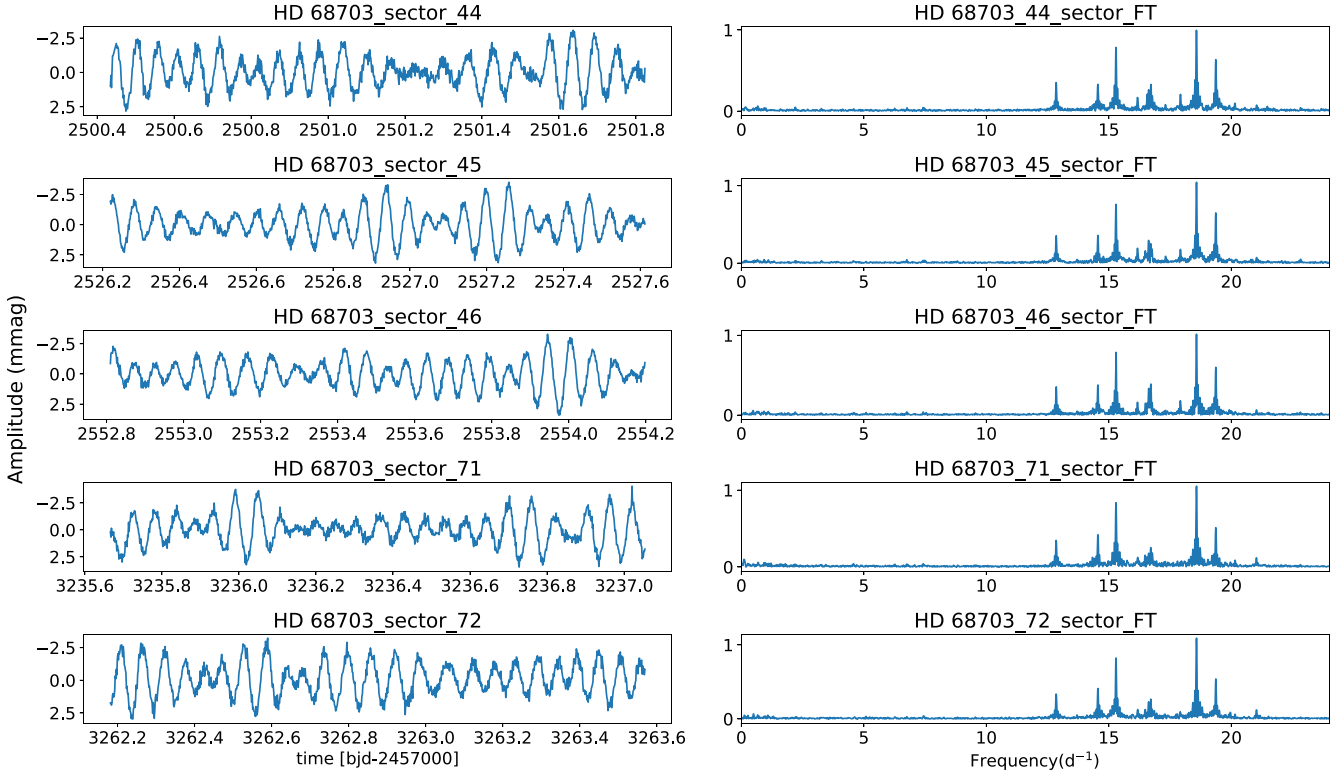

Figure A4. The light curves (left panels) and corresponding frequency spectra (right panels) for HD 68703 obtained with *TESS* in Sectors 44, 45, 46, 71, and 72 (from top to bottom row). We plot only up to 24 d^{-1}, since no significant frequency was found beyond this point.

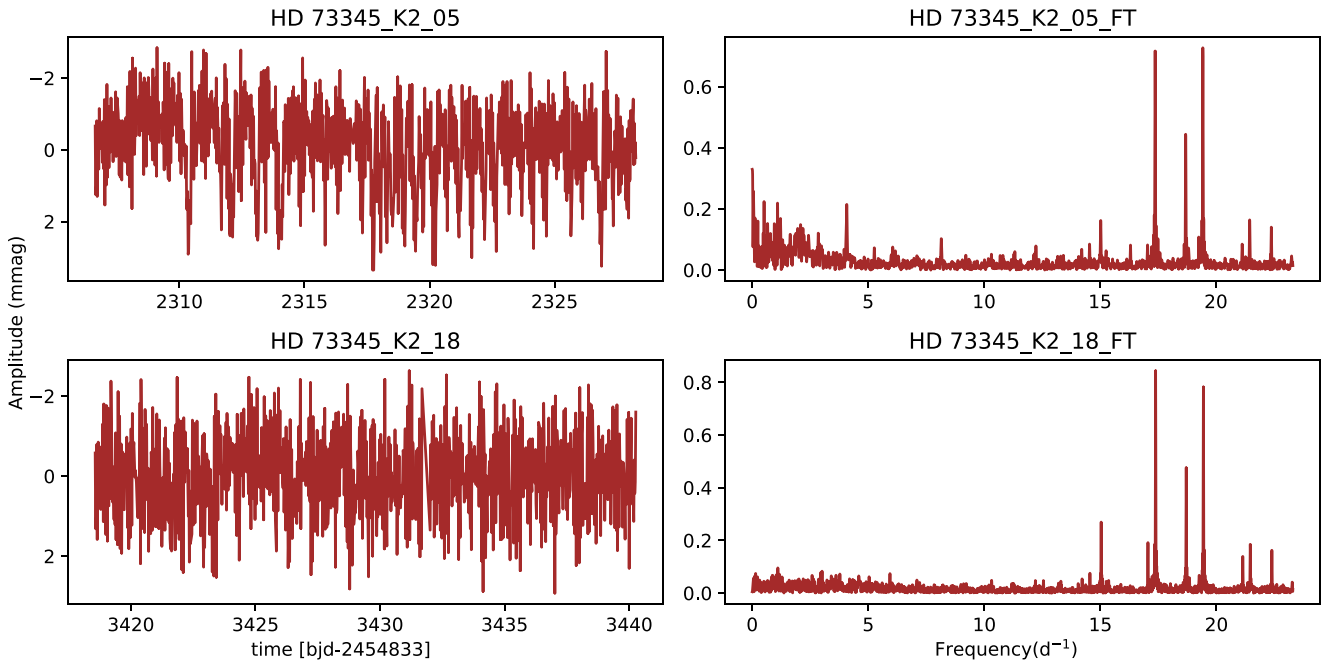

Figure A5. The light curves (left panels) and corresponding frequency spectra (right panels) for HD 73345 obtained with *K2* in Campaign 5 (top row) and Campaign 18 (bottom row).

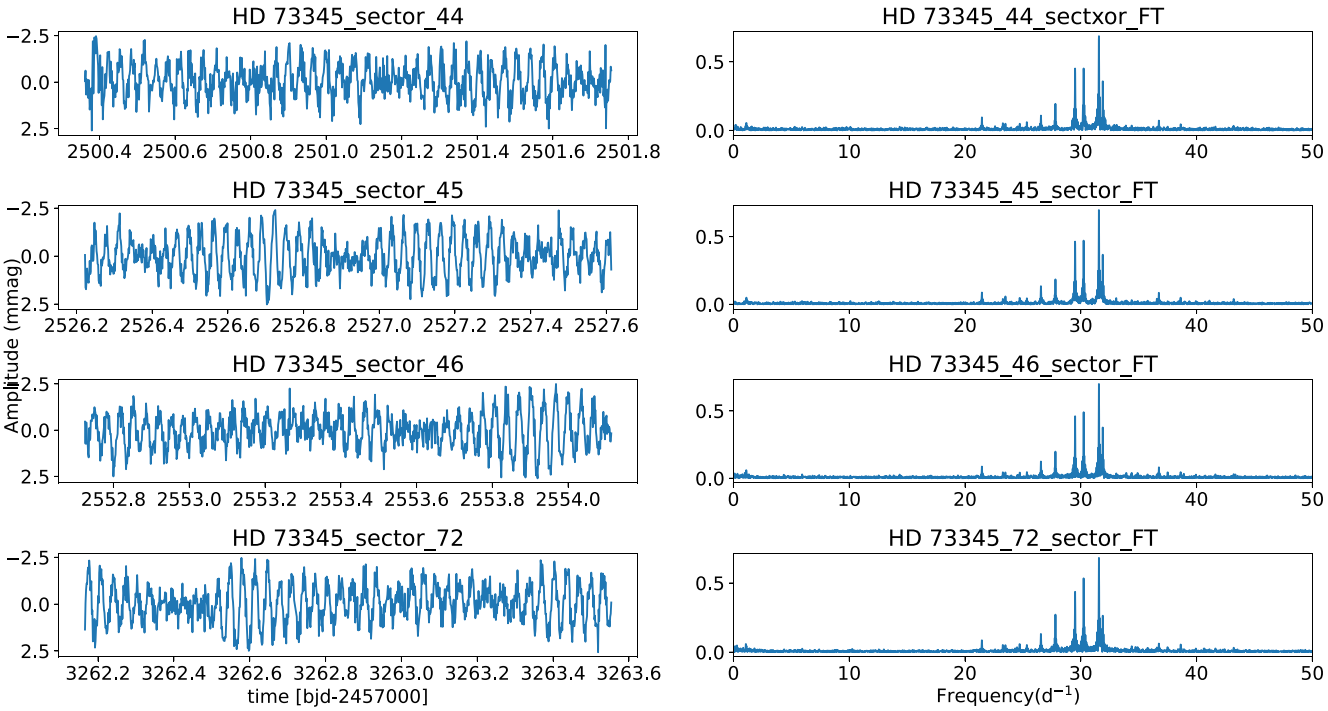

Figure A6. The light curves (left panels) and corresponding frequency spectra (right panels) for HD 73345 obtained with *TESS* in Sectors 44, 45, 46, and 72 (from top to bottom row). We plot only up to 50 d^{-1} as no significant frequencies were found beyond this range. The noticeable asymmetry in the light curves may be attributed to the interaction of two closely spaced frequencies.

APPENDIX B: FREQUENCY SOLUTIONS FROM *TESS* AND *K2* TIME-SERIES ANALYSIS

Table B1. The frequencies, corresponding amplitudes, and SNRs for HD 23734 derived from three consecutive sectors (42, 43, and 44) of *TESS* time-series data. The frequency solution based on the *K2* data from Campaign 4 is also listed. Pulsation constants (Q) are provided for the identified radial modes. Only the short-cadence *TESS* data were used in this analysis to avoid aliasing effects and to resolve frequencies beyond the Nyquist (Nyq) limit inherent to *K2* long-cadence data.

	TESS					*K2*			
	f (d^{-1})	Amp (±0.003 mmag)	SNR	Q-value (d)	Comb. freqs.		f (d^{-1})	Amp (±0.1 mmag)	SNR
f_{T1}	22.90016±0.00001	1.727	309.8	–	–	f_{K1}	22.9001±0.0007	1.1	22.0
f_{T2}	25.60789±0.00003	0.936	175.4	–	–	2Nyq-f_{K2}	25.608±0.001	0.5	10.7
f_{T3}	16.13569±0.00004	0.662	126.6	–	–	f_{K3}	16.136±0.002	0.5±0.1	9.1
f_{T4}	38.94782±0.00006	0.446	75.7	0.017 ± 0.003	$F4$	–	–	–	–
f_{T5}	30.78033±0.00008	0.308	58.4	–	–	–	–	–	–
f_{T6}	38.79358±0.00009	0.286	49.0	–	–	–	–	–	–
f_{T7}	32.93878±0.00009	0.265	42.1	0.02 ± 0.004	$F3$	–	–	–	–
f_{T8}	42.4168±0.0001	0.246	44.3	–	–	–	–	–	–
f_{T9}	22.5310±0.0001	0.221	40.8	–	–	–	–	–	–
f_{T10}	25.7210±0.0001	0.208	39.4	–	–	–	–	–	–
f_{T11}	42.9315±0.0001	0.185	31.1	–	–	–	–	–	–
f_{T12}	33.0666±0.0002	0.160	24.3	–	–	–	–	–	–
f_{T13}	29.8766±0.0002	0.165	29.6	–	–	–	–	–	–
f_{T14}	42.2087±0.0002	0.164	29.5	–	–	–	–	–	–
f_{T15}	22.0017±0.0002	0.160	28.8	–	–	–	–	–	–
f_{T16}	19.2192±0.0002	0.156	30.8	–	–	–	–	–	–
f_{T17}	32.2210±0.0002	0.141	22.2	–	–	–	–	–	–
f_{T18}	33.9091±0.0002	0.131	24.4	–	–	–	–	–	–
f_{T19}	39.5157±0.0002	0.124	20.6	–	–	–	–	–	–
f_{T20}	41.7995±0.0002	0.128	23.1	–	–	–	–	–	–
f_{T21}	49.9145±0.0002	0.117	18.6	–	–	–	–	–	–
f_{T22}	26.0984±0.0002	0.101	18.5	–	–	–	–	–	–
f_{T23}	44.0720±0.0003	0.096	16.3	–	–	–	–	–	–
f_{T24}	22.4092±0.0003	0.091	16.6	–	–	–	–	–	–
f_{T25}	49.0387±0.0003	0.087	12.3	–	–	–	–	–	–
f_{T26}	37.7358±0.0003	0.086	15.7	–	–	–	–	–	–
f_{T27}	36.3113±0.0003	0.082	12.6	–	–	–	–	–	–
f_{T28}	27.5403±0.0003	0.080	15.0	–	–	–	–	–	–
f_{T29}	42.0281±0.0003	0.078	14.0	–	–	–	–	–	–
f_{T30}	31.1892±0.0003	0.074	13.6	–	–	–	–	–	–
f_{T31}	54.7124±0.0003	0.074	12.5	–	–	–	–	–	–
f_{T32}	34.3933±0.0004	0.070	11.6	–	–	–	–	–	–
f_{T33}	24.9947±0.0004	0.064	11.2	–	–	–	–	–	–
f_{T34}	46.4479±0.0004	0.063	9.9	–	–	–	–	–	–
f_{T35}	40.8229±0.0004	0.056	10.3	–	–	–	–	–	–
f_{T36}	43.8136±0.0004	0.056	9.1	–	–	–	–	–	–
f_{T37}	52.5559±0.0005	0.054	9.0	–	–	–	–	–	–
f_{T38}	29.2187±0.0004	0.056	11.9	–	–	–	–	–	–
f_{T39}	29.0548±0.0005	0.053	11.1	–	–	–	–	–	–
f_{T40}	49.5389±0.0005	0.053	8.1	–	–	–	–	–	–
f_{T41}	28.3355±0.0005	0.051	10.9	–	–	–	–	–	–
f_{T42}	21.6257±0.0005	0.051	9.7	–	–	–	–	–	–
f_{T43}	18.7759±0.0005	0.046	9.2	–	–	–	–	–	–
f_{T44}	33.3351±0.0005	0.045	7.0	–	–	–	–	–	–
f_{T45}	54.5173±0.0006	0.045	7.2	–	–	–	–	–	–
f_{T46}	18.3873±0.0006	0.044	8.8	–	–	–	–	–	–
f_{T47}	30.3839±0.0006	0.045	8.3	–	–	–	–	–	–
f_{T48}	29.6660±0.0006	0.044	8.5	–	–	–	–	–	–
f_{T49}	31.7962±0.0006	0.043	7.0	–	–	–	–	–	–
f_{T50}	46.0459±0.0006	0.041	6.9	–	–	–	–	–	–
f_{T51}	10.3633±0.0006	0.041	9.7	–	–	–	–	–	–
f_{T52}	37.0475±0.0006	0.040	7.6	–	–	–	–	–	–
f_{T53}	41.4372±0.0006	0.039	7.1	–	–	–	–	–	–
f_{T54}	36.1861±0.0006	0.039	5.8	–	–	–	–	–	–

Table B1 *continued*

	TESS						*K2*		
	f (d^{-1})	Amp ($\pm$0.003 mmag)	SNR	Q-value (d)	Comb. freqs.		f (d^{-1})	Amp ($\pm$0.1 mmag)	SNR
f_{T55}	56.1051$\pm$0.0006	0.038	6.5	–	–	–	–	–	–
f_{T56}	50.8394$\pm$0.0006	0.039	7.2	–	–	–	–	–	–
f_{T57}	37.4168$\pm$0.0006	0.038	6.9	–	–	–	–	–	–
f_{T58}	21.6767$\pm$0.0006	0.039	7.2	–	–	–	–	–	–
f_{T59}	47.1537$\pm$0.0007	0.037	6.4	–	–	–	–	–	–
f_{T60}	12.3188$\pm$0.0007	0.037	7.1	–	–	–	–	–	–
f_{T61}	18.9915$\pm$0.0007	0.037	7.4	–	–	–	–	–	–
f_{T62}	52.8368$\pm$0.0007	0.036	5.6	–	–	–	–	–	–
f_{T63}*	2.3406$\pm$0.0007	0.034	4.8	–	$F_{\rm rot}$	–	–	–	–
f_{T64}*	4.660$\pm$0.001	0.018	3.5	–	$2F_{\rm rot}$	–	–	–	–

Notes. The column 'comb. freqs.' indicates the identified radial modes, rotational frequency, and their combinations. *Fn*: frequency of radial mode with order n; $F_{\rm rot}$: rotational frequency; '$*$': frequencies with SNR < 5.2, but potentially corresponding to the rotational frequency or its harmonic.

Table B2. Same as Table B1, but for HD 68703. In this case, we combined the consecutive *TESS* Sectors 44, 45, and 46, along with the *K2* light curves from Campaigns 5 and 18. No frequencies beyond the *K2* Nyquist limit were detected in this analysis.

	TESS						*K2*		
	f (d^{-1})	Amp ($\pm$0.002 mmag)	SNR	Q-value (d)	Comb. freqs.		f (d^{-1})	Amp ($\pm$0.006 mmag)	SNR
f_{T1}	18.57798$\pm$0.00001	1.032	246.9	0.016$\pm$0.003	$F4$	f_{K4}	18.577989$\pm$0.000006	0.0189	69.9
f_{T2}	15.29221$\pm$0.00002	0.783	179.3	0.020$\pm$0.003	$F3$	f_{K1}	15.292443$\pm$0.000004	0.737	119.6
f_{T3}	19.36695$\pm$0.00002	0.641	145.0	–	–	f_{K3}	19.366866$\pm$0.000006	0.481	63.1
f_{T4}	14.55409$\pm$0.00003	0.365	106.9	–	–	f_{K6}	14.55414$\pm$0.00001	0.268	48.7
f_{T5}	12.85130$\pm$0.00003	0.358	127.5	–	$F1 + 3F_{\rm rot}$	f_{K8}	12.85119$\pm$0.00001	0.207	48.3
f_{T6}	16.70863$\pm$0.00004	0.326	83.2	–	–	f_{K5}	16.709372$\pm$0.000007	0.385	50.9
f_{T7}	16.63107$\pm$0.00004	0.328	82.9	–		f_{K2}	16.632078$\pm$0.000004	0.645	84.5
f_{T8}	17.92033$\pm$0.00007	0.188	47.8	–	–	f_{K7}	17.92044$\pm$0.00001	0.213	35.4
f_{T9}	16.17536$\pm$0.00009	0.139	33.0	–	–	f_{K9}	16.17520$\pm$0.00002	0.180	22.4
f_{T10}	21.0273$\pm$0.0002	0.077	17.1	–	$2F3–F1$	–	–	–	–
f_{T11}	16.4889$\pm$0.0002	0.072	17.9	–	–	–	–	–	–
f_{T12}	17.3132$\pm$0.0002	0.065	18.5	–	–	f_{K13}	17.31204$\pm$0.00004	0.078	10.6
f_{T13}	19.9153$\pm$0.0002	0.050	11.4	–	–	–	–	–	–
f_{T14}	20.1599$\pm$0.0002	0.052	12.6	–	–	–	–	–	–
f_{T15}	13.6909$\pm$0.0003	0.046	16.8	–	–	f_{K18}	13.69112$\pm$0.00005	0.058	11.4
f_{T16}	22.8251$\pm$0.0003	0.044	12.7	–	–	–	–	–	–
f_{T17}	0.9242$\pm$0.0003	0.042	7.0	–	–	–	–	–	–
f_{T18}	0.6464$\pm$0.0003	0.039	6.3	–	–	–	–	–	–
f_{T19}	19.9664$\pm$0.0003	0.041	9.4	–	–	–	–	–	–
f_{T20}	0.4850$\pm$0.0003	0.042	6.7	–	–	–	–	–	–
f_{T21}	6.7560$\pm$0.0003	0.040	11.8	–	–	–	–	–	–
f_{T22}	2.1989$\pm$0.0003	0.039	9.4	–	$2F_{\rm rot}$	–	–	–	–
f_{T23}	7.4194$\pm$0.0003	0.038	12.2	–	–	–	–	–	–
f_{T24}	17.3882$\pm$0.0003	0.036	10.0	–	-	–	–	–	–
f_{T25}	16.1046$\pm$0.0003	0.039	9.3	–	–	–	–	–	–
f_{T26}	1.0995$\pm$0.0004	0.033	5.9	–	$F_{\rm rot}$	–	–	–	–
f_{T27}	17.8126$\pm$0.0004	0.032	8.6	–	–	–	–	–	–
f_{T28}	21.4722$\pm$0.0004	0.030	7.1	–	–	–	–	–	–
f_{T29}	19.8069$\pm$0.0004	0.031	7.3	–	–	f_{K17}	19.80777$\pm$0.00005	0.061	8.4
f_{T30}	19.6983$\pm$0.0004	0.030	7.3	–	$F4 + F_{\rm rot}$, $F3 + 4F_{\rm rot}$	–	–	–	–
f_{T31}	3.2738$\pm$0.0005	0.027	7.6	–	$3F_{\rm rot}$, $F4–F3$	–	–	–	–
f_{T32}	4.5788$\pm$0.0005	0.027	6.8	–	–	–	–	–	–
f_{T33}	20.5333$\pm$0.0005	0.027	6.0	–	–	–	–	–	–
f_{T34}	17.5449$\pm$0.0005	0.027	7.2	–	–	–	–	–	–
f_{T35}	23.6716$\pm$0.0005	0.023	6.6	–	–	–	–	–	–
f_{T36}	9.5603$\pm$0.0007	0.018	6.5	0.031$\pm$0.005	$F1$	–	–	–	–
-	–	–	–	–	–	f_{K15}	16.58560$\pm$0.00004	0.076	9.8
-	–	–	–	–	–	f_{K16}	19.13116$\pm$0.00004	0.063	8.9

Table B3. Same as Table B1, but for HD 73345. The frequency solution is given here is on combining the consecutive *TESS* Sectors 44, 45, and 46 and *K2* time-series for the Campaigns 5 and 18.

	TESS					*K2*			
	f (d^{-1})	Amp (±0.003 mmag)	SNR	Q-value	Comb. freqs		f	Amp (±0.006 mmag)	SNR
f_{T1}	31.56558±0.00003	0.694	154.0	–	–	2Nyq-f_{K1}	31.56564±0.00001	0.285	107.2
f_{T2}	30.24686±0.00005	0.473	108.4	–	–	2Nyq-f_{K3}	30.24688±0.00001	0.203	77.0
f_{T3}	29.50692±0.00005	0.458	112.1	0.014 ± 0.002	$F4$	2Nyq-f_{K2}	29.50709±0.00001	0.331	130.0
f_{T4}	31.89596±0.00006	0.372	80.8	–	–	2Nyq-f_{K7}	31.89610±0.00004	0.064	22.6
f_{T5}	27.8107±0.0001	0.191	42.0	–	–	2Nyq-f_{K8}	27.80985±0.00006	0.048	19.7
f_{T6}	26.5554±0.0002	0.123	27.2	–	–	2Nyq-f_{K6}	26.55562±0.00004	0.066	24.8
f_{T7}	21.4556±0.0003	0.089	22.8	–	–	f_{K5}	21.45574±0.00003	0.081	32.6
f_{T8}	36.7432±0.0003	0.081	20.3	–	–	–	–	–	–
f_{T9}	1.1119±0.0004	0.055	8.1	–	$F_{\rm rot}$	–	–	–	–
f_{T10}	25.3400±0.0004	0.051	11.7	–	–	2Nyq-f_{K13}	25.34047±0.00008	0.032	10.5
f_{T11}	23.4880±0.0005	0.047	11.3	–	–	f_{K9}	23.48595±0.00008	0.035	12.2
f_{T12}	24.7246±0.0005	0.047	10.8	0.017 ± 0.002	$F3$	2Nyq-f_{K10}	24.72477±0.00008	0.035	11.8
f_{T13}	38.6261±0.0005	0.046	9.8	–	–	–	–	–	–
f_{T14}	23.2674±0.0005	0.045	10.8	–	–	–	–	–	–
f_{T15}	34.3951±0.0007	0.034	6.4	0.012 ± 0.002	$F5$	2Nyq-f_{K12}	34.39525±0.00008	0.034	10.7
f_{T16}	33.0620±0.0007	0.034	7.0	–	–	–	–	–	–
f_{T17}	43.2062±0.0007	0.033	7.6	–	–	–	–	–	–
f_{T18}	37.5039±0.0008	0.030	7.2	–	–	–	–	–	–
f_{T19}	36.5739±0.0008	0.029	7.4	–	–	–	–	–	–
f_{T20}	35.7724±0.0009	0.027	5.8	–	–	–	–	–	–
f_{T21}	10.095±0.001	0.022	5.6	–	–	–	–	–	–
f_{T22}	14.360±0.001	0.022	5.4	–	$3F4$–$3F3$	f_{K19}	14.2104±0.0001	0.022	7.0
-	–	–	–	–	–	f_{K4}	15.03217±0.00001	0.210	67.9
-	–	–	–	–	–	f_{K11}	19.25318±0.00008	0.035	14.1
-	–	–	–	–	–	f_{K15}	18.8381±0.0001	0.025	9.3
-	–	–	–	–	–	f_{K16}	8.1570±0.0001	0.023	6.0

APPENDIX C: LSD PROFILES VARIATIONS

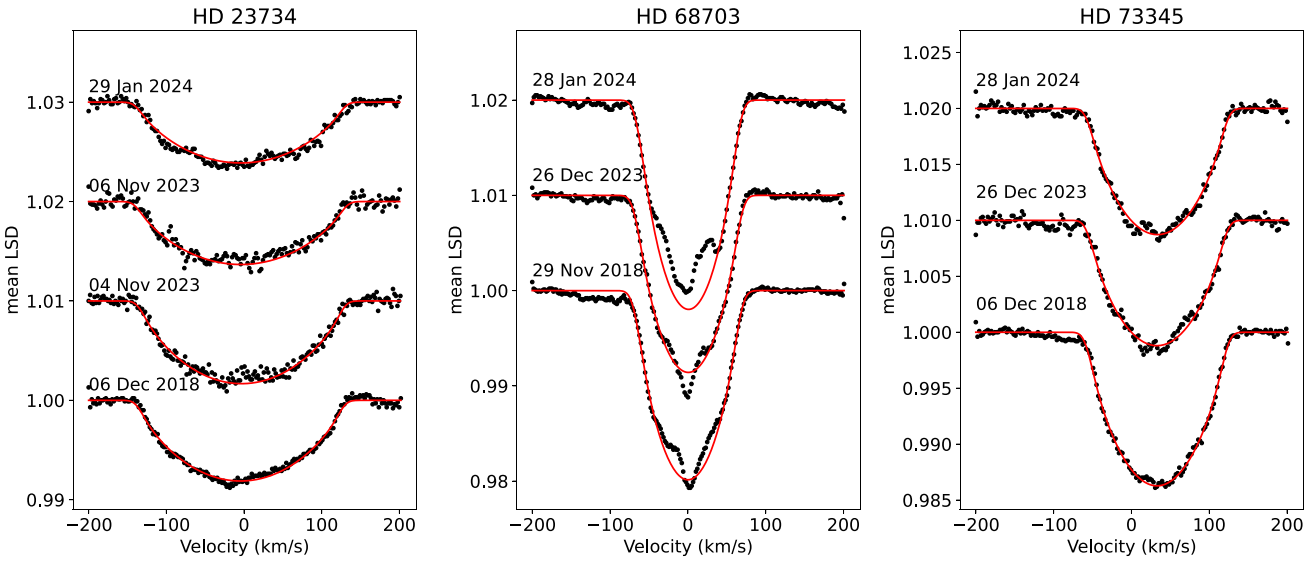

Figure C1. Left panel: mean LSD profiles of HD 23734 obtained from spectra taken on four different nights. The broadening of the LSD indicates a high rotational velocity, consistent with values listed in Table 2. Middle and right panels:L SD profiles of HD 68703 and HD 73345, respectively, based on observations from three separate nights. Distinct line profile variations are evident in both cases. In all panels, the red curves represent the best-fitting rotational broadening profiles. All thee spectra were acquired using HESP mounted on HCT.

APPENDIX D: ROTATION

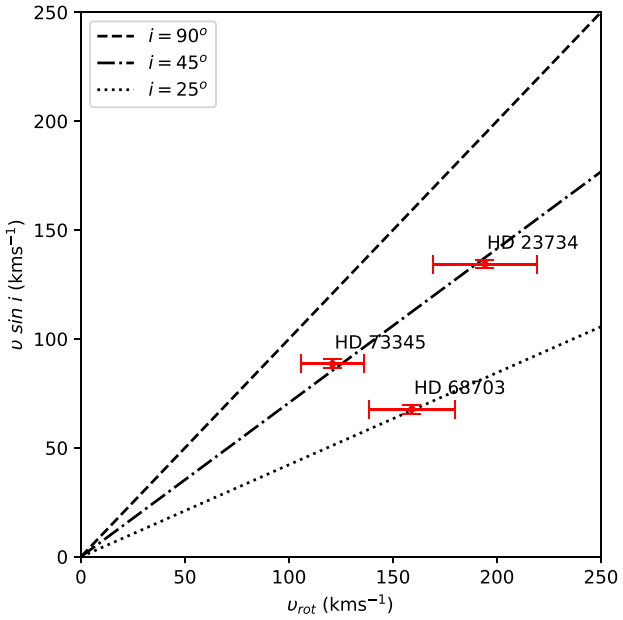

Figure D1. Relationship between the equatorial rotational velocity $\upsilon_{\rm rot}$ derived from the selected rotational frequency of each star and the corresponding $\upsilon \sin i$ values determined from spectroscopy. The dashed, dash–dotted, and dotted lines corresponds to inclinations of 90°, 45°, and 25°, respectively.

APPENDIX E: FLUX DEPRESSION AND STRENGTH OF CA-K LINES

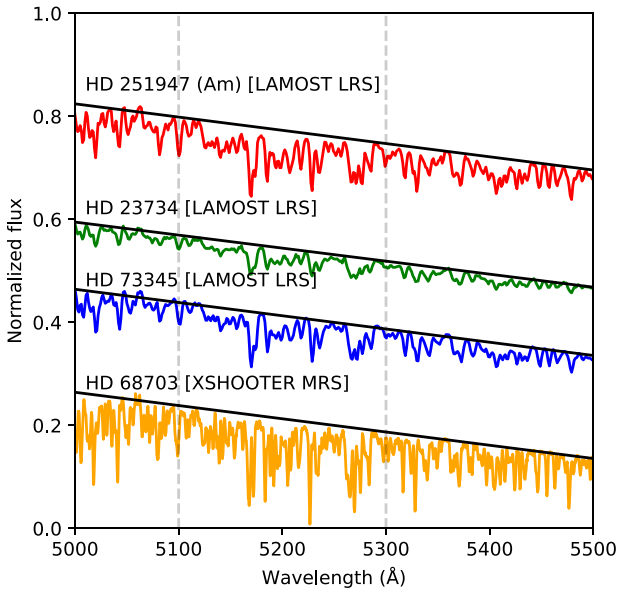

Figure E1. Flux-calibrated low-resolution LAMOST spectra of HD 23734 and HD 73345 (both from DR-10). We could not find a flux-calibrated LAMOST spectrum of HD 68703 in any of the available data releases, therefore, we took flux-calibrated medium-resolution spectra of HD 68703 obtained by XSHOOTER. For the comparison, flux-calibrated LAMOST spectra of a known Am star HD 251947 (DR-10) is also shown. The individual spectrum has been vertically offset for clarity. No indication of a flux depression around 5200 Å (enclosed by two vertical black dashed lines) is observed, providing further evidence of the non-peculiar nature of our sample.

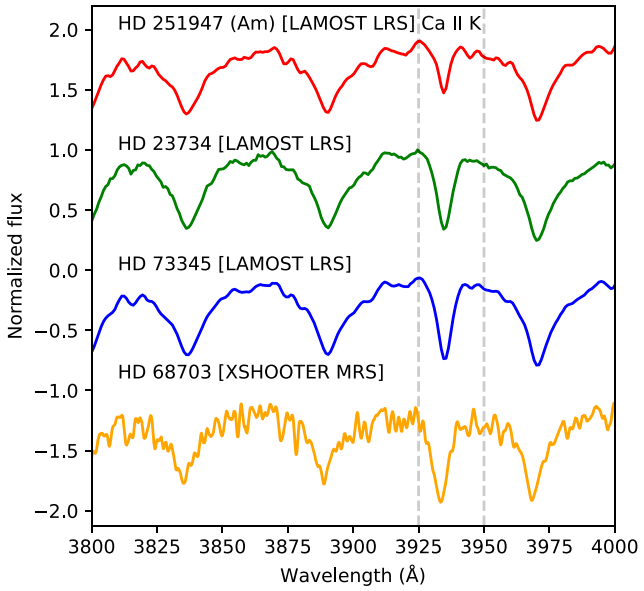

Figure E2. Comparison of the strength of Ca II K lines for HD 23734 and HD 73345 from LAMOST low-resolution spectra with a known Am star HD 251947 of similar spectral type. Since no LAMOST LRS spectrum is available for HD 68703, hence, we illustrate the medium-resolution XSHOOTER spectrum instead. From this figure, it is evident that the strength of Ca II K lines is normal in our target stars, while the strength of the known Am star, HD 251947 is weak indicating that the studied stars are chemically normal.

This paper has been typeset from a TEX/LATEX file prepared by the author.